

OPTIMIZATION OF IMAGING TECHNIQUES FOR BACKGROUND
SUPPRESSION OF STELLAR NUCLEO-SYNTHESIS REACTIONS
WITH I-TED

CHARACTERISATION, UPGRADES AND OUTLOOK



Bernardo Bernardino Gameiro

Erasmus Mundus Joint Master Degree on Nuclear Physics (EMJMD-NucPhys)
Departamento de Física Atómica, Molecular y Nuclear
Facultad de Física
Universidad de Sevilla

2023/02-2023/09 -- v2023-09-05

Código seguro de Verificación : GEN-d21c-d2af-ba88-99ce-da2f-70ae-e905-5e92 | Puede verificar la integridad de este documento en la siguiente dirección :
<https://portafirmas.redsara.es/pf/valida>



CSV : GEN-d21c-d2af-ba88-99ce-da2f-70ae-e905-5e92

DIRECCIÓN DE VALIDACIÓN : <https://portafirmas.redsara.es/pf/valida>

FIRMANTE(1) : BERNARDO BERNARDINO GAMEIRO | FECHA : 09/11/2023 15:40 | NOTAS : F

FIRMANTE(2) : JORGE LERENDEGUI MARCO | FECHA : 09/11/2023 18:46 | NOTAS : CF

Bernardo Bernardino Gameiro: *Optimization of imaging techniques for background suppression of stellar Nucleo-Synthesis reactions with i-TED*,
Characterisation, Upgrades and Outlook, © 2023/02-2023/09

SUPERVISORS:

Carlos Guerrero, US
Jorge Lerendegui Marco, IFIC-UV
Javier Balibrea Correa, IFIC-UV

LOCATION:

Instituto de Física Corpuscular - Universitat de València

TIME FRAME:

2023/02-2023/09



CSV : GEN-d21c-d2af-ba88-99ce-da2f-70ae-e905-5e92

DIRECCIÓN DE VALIDACIÓN : <https://portafirmas.redsara.es/pf/valida>

FIRMANTE(1) : BERNARDO BERNARDINO GAMEIRO | FECHA : 09/11/2023 15:40 | NOTAS : F

FIRMANTE(2) : JORGE LERENDEGUI MARCO | FECHA : 09/11/2023 18:46 | NOTAS : CF

Estar preparado es la mitad de la victoria.

-- Miguel de Cervantes

Che, non men che saver, dubbiar m'aggrata.

-- Dante Alighieri

Dedicated to my supportive family
and all the friends I've made in the last 2 years.



CSV : GEN-d21c-d2af-ba88-99ce-da2f-70ae-e905-5e92

DIRECCIÓN DE VALIDACIÓN : <https://portafirmas.redsara.es/pf/valida>

FIRMANTE(1) : BERNARDO BERNARDINO GAMEIRO | FECHA : 09/11/2023 15:40 | NOTAS : F

FIRMANTE(2) : JORGE LERENDEGUI MARCO | FECHA : 09/11/2023 18:46 | NOTAS : CF

Código seguro de Verificación : GEN-d21c-d2af-ba88-99ce-da2f-70ae-e905-5e92 | Puede verificar la integridad de este documento en la siguiente dirección :
<https://portafirmas.redsara.es/pf/valida>



CSV : GEN-d21c-d2af-ba88-99ce-da2f-70ae-e905-5e92

DIRECCIÓN DE VALIDACIÓN : <https://portafirmas.redsara.es/pf/valida>

FIRMANTE(1) : BERNARDO BERNARDINO GAMEIRO | FECHA : 09/11/2023 15:40 | NOTAS : F

FIRMANTE(2) : JORGE LERENDEGUI MARCO | FECHA : 09/11/2023 18:46 | NOTAS : CF

ABSTRACT

The work presented in this thesis refers to the upgrade and characterization of the multi Total-Energy Detector with imaging capability (**i-TED**) detector system with subsequent studies of its background suppression capabilities.

The multi **i-TED** is an innovative γ -ray imaging system consisting of an array of four Compton cameras.

This thesis is divided into introduction, the two parts of the project, conclusion, and appendix.

The data-driven upgrade of the **i-TED** modules and the subsequent characterization of its performance, **Part ii**. This includes characterization of the energy resolution, **Section 4.3.1.1**; timing, **Section 4.2.3**; coincidence energy resolution, **Section 4.3.1.2**; dependence on temperature, **Section 4.2.5**; and alpha activity, **Section 4.3.3**.

The imaging studies, **Part iii**, were performed with the objectives of the detector in mind, **Chapter 6**. The background suppression, **Section 8.2**, and imaging resolution, **Section 8.1**, studies were conducted using sources at Instituto de Física Corpuscular (**IFIC**) and in a scientific campaign at Centre for Micro Analysis of Materials (**CMAM**) in June 2023.

v



CSV : GEN-d21c-d2af-ba88-99ce-da2f-70ae-e905-5e92

DIRECCIÓN DE VALIDACIÓN : <https://portafirmas.redsara.es/pf/valida>

FIRMANTE(1) : BERNARDO BERNARDINO GAMEIRO | FECHA : 09/11/2023 15:40 | NOTAS : F

FIRMANTE(2) : JORGE LERENDEGUI MARCO | FECHA : 09/11/2023 18:46 | NOTAS : CF

Código seguro de Verificación : GEN-d21c-d2af-ba88-99ce-da2f-70ae-e905-5e92 | Puede verificar la integridad de este documento en la siguiente dirección :
<https://portafirmas.redsara.es/pf/valida>



CSV : GEN-d21c-d2af-ba88-99ce-da2f-70ae-e905-5e92

DIRECCIÓN DE VALIDACIÓN : <https://portafirmas.redsara.es/pf/valida>

FIRMANTE(1) : BERNARDO BERNARDINO GAMEIRO | FECHA : 09/11/2023 15:40 | NOTAS : F

FIRMANTE(2) : JORGE LERENDEGUI MARCO | FECHA : 09/11/2023 18:46 | NOTAS : CF

*Theory and practice sometimes clash.
And when that happens, theory loses.
Every single time.*

-- Linus Torvalds

*All the good experimental physicists I have known
have had an intense curiosity
that no Keep Out sign could mute.*

-- Luis Walter Alvarez

ACKNOWLEDGMENTS

HYMNS-ERC The work was developed as part of the Gamma-ray and Neutron Spectroscopy group of **IFIC**, under the High-sensitivity Measurements of key stellar Nucleo-Synthesis reactions (**HYMNS**) project funded by the European Research Council (**ERC**). As such I would like to thank everyone in the group for giving me the opportunity of taking this project and for the guidance and feedback throughout.

FINDING A THESIS I would like to thank Professor Arias, former coordinator of the Erasmus Mundus Joint Master Degree on Nuclear Physics (**EMJMD-NucPhys**), for putting me in contact with the research groups of **IFIC**. Without your help I wouldn't have been able to undergo this project.

TEMPLATE I would like to thank André Miede and Ivo Pletikosić for making the current **L^AT_EXtemplate** available under the **GNU GPL v2** license.



CSV : GEN-d21c-d2af-ba88-99ce-da2f-70ae-e905-5e92

DIRECCIÓN DE VALIDACIÓN : <https://portafirmas.redsara.es/pf/valida>

FIRMANTE(1) : BERNARDO BERNARDINO GAMEIRO | FECHA : 09/11/2023 15:40 | NOTAS : F

FIRMANTE(2) : JORGE LERENDEGUI MARCO | FECHA : 09/11/2023 18:46 | NOTAS : CF

Código seguro de Verificación : GEN-d21c-d2af-ba88-99ce-da2f-70ae-e905-5e92 | Puede verificar la integridad de este documento en la siguiente dirección :
<https://portafirmas.redsara.es/pf/valida>



CSV : GEN-d21c-d2af-ba88-99ce-da2f-70ae-e905-5e92

DIRECCIÓN DE VALIDACIÓN : <https://portafirmas.redsara.es/pf/valida>

FIRMANTE(1) : BERNARDO BERNARDINO GAMEIRO | FECHA : 09/11/2023 15:40 | NOTAS : F

FIRMANTE(2) : JORGE LERENDEGUI MARCO | FECHA : 09/11/2023 18:46 | NOTAS : CF

CONTENTS

I Introduction & Theory	
1 Introduction	3
1.1 Nuclear Astrophysics	3
1.1.1 Nucleosynthesis	3
1.1.2 Neutron capture processes	4
1.1.3 Neutron time-of-flight experiments	5
1.1.4 Challenges	6
1.2 Interaction of radiation with matter	7
1.2.1 Compton scattering	7
1.2.2 Scintillators	8
2 i-TED	11
2.1 Total Energy Detectors	11
2.1.1 Conditions for the TED technique	11
2.1.2 Experimental techniques for TED	12
2.2 Evolution of gamma-ray Scintillation Detectors	12
2.2.1 Materials	13
2.2.2 Geometries	13
2.3 Gamma-ray imaging detectors	14
2.3.1 Compton cameras	14
2.3.2 PET	15
2.4 The multi i-TED detector system	16
2.4.1 Main components	16
2.4.2 Requirements and innovative aspects	18
2.4.3 Data acquisition	20
3 Applications of i-TED	21
3.1 Scientific Applications	21
3.1.1 Neutron capture measurements of astrophysical interest	21
3.2 Industrial Applications	21
3.2.1 Range verification in proton therapy	21
3.2.2 Nuclear waste analysis	22
II Detector upgrades and characterization	
4 Multi i-TED detector system	27
4.1 Initial status	27
4.2 Hardware and software upgrades	28
4.2.1 Pixel response and position reconstruction	28
4.2.2 Pixel threshold optimization	31
4.2.3 Timing	33
4.2.4 Energy resolution	37
4.2.5 Temperature	38

CSV : GEN-d21c-d2af-ba88-99ce-da2f-70ae-e905-5e92

DIRECCIÓN DE VALIDACIÓN : <https://portafirmas.redsara.es/pf/valida>

FIRMANTE(1) : BERNARDO BERNARDINO GAMEIRO | FECHA : 09/11/2023 15:40 | NOTAS : F

FIRMANTE(2) : JORGE LERENDEGUI MARCO | FECHA : 09/11/2023 18:46 | NOTAS : CF




4.3	Characterization	39
4.3.1	Energy resolution	39
4.3.2	Counting rate	40
4.3.3	Alpha activity	41
5	i-TED-E	43
5.1	Motivation	43
5.2	Characterization of i-TED-E	44
5.2.1	Energy resolution	44
5.2.2	Counting rate	45
5.2.3	Alpha activity	45
III Imaging and background discrimination		
6	Imaging Objectives of i-TED	49
6.1	Background Suppression	49
6.2	Source Visualization	50
7	Compton Imaging Techniques	51
7.1	Imaging Algorithms	51
7.1.1	Back-Projection	51
7.1.2	Analytical	52
7.1.3	Stochastic Ensemble Origin	52
7.1.4	Resolution Recovery	52
7.2	Figures of Merit	53
7.2.1	Lambda	53
7.2.2	Angular Resolution Measure	53
8	Imaging Studies with i-TED	55
8.1	Characterization of the imaging performance	55
8.1.1	Characterization of imaging for i-TED-E	55
8.2	Discrimination between events in different positions	56
8.2.1	Feature selection and outlook for Machine Learning (ML) studies	59
IV Conclusion		
9	Summary	65
9.1	Detector upgrades and characterization	65
9.1.1	Starting point and upgrades	65
9.1.2	i-TED-E	66
9.2	Imaging studies	66
9.2.1	Characterization of the imaging performance	66
9.2.2	Discrimination between events in different positions	66
V Appendix		
A	Future developments based on the i-TED concept	69
A.1	GN-Vision	69
A.1.1	Applicability for neutron captures of astrophysical interest	69



- A.2 i-TED with Anti-Compton Shield 69
- B Complementary material of the characterization 71
 - B.1 Detector upgrades and characterization 71
 - B.2 Imaging and background discrimination 72
- C Software developed 75
 - c.1 Scientific Data Management 75
 - c.2 Calibration Software 77
 - c.2.1 Developed version 77
 - c.2.2 InterSpec 78
 - c.3 Rewrite of singles2tree 79
 - c.3.1 i-TED's data processing 79
 - c.3.2 Software upgrades 81
 - c.3.3 Proposed software upgrades 81

Código seguro de Verificación : GEN-d21c-d2af-ba88-99ce-da2f-70ae-e905-5e92 | Puede verificar la integridad de este documento en la siguiente dirección : <https://portafirmas.redsara.es/pf/valida>



CSV : GEN-d21c-d2af-ba88-99ce-da2f-70ae-e905-5e92
 DIRECCIÓN DE VALIDACIÓN : <https://portafirmas.redsara.es/pf/valida>
FIRMANTE(1) : BERNARDO BERNARDINO GAMEIRO | FECHA : 09/11/2023 15:40 | NOTAS : F
FIRMANTE(2) : JORGE LERENDEGUI MARCO | FECHA : 09/11/2023 18:46 | NOTAS : CF

LIST OF FIGURES

Figure 1.1	Scheme of the neutron-capture processes, including the s-process path, relevant for the motivation of the present work. From [5].	4
Figure 1.2	Scheme of a neutron time of flight experiment. From [6].	5
Figure 1.3	Neutron Time-of-Flight facility (<i>nToF</i>) experiment at European Organization for Nuclear Research (<i>CERN</i>). From [10].	6
Figure 1.4	Interaction mechanisms of electromagnetic radiation with matter.	7
Figure 1.5	Scattering according to the formula of Klein-Nishina for several γ -ray energies that will be used in this work for the characterization of <i>i-TED</i>	8
Figure 2.1	Scheme of a neutron capture to an excited state and possible decays to ground state by emission of different γ -ray cascades.	11
Figure 2.2	Measured energy resolution of several scintillators for 662 keV gamma rays as a function of their light output. From [18].	13
Figure 2.3	Illustration of Compton imaging through overlapping Compton cones. From [24].	14
Figure 2.4	Illustration of Positron-Electron Tomography (<i>PET</i>) and Time-of-Flight (<i>ToF</i>) <i>PET</i> . From [26].	15
Figure 2.5	The scheme of the original concept, [32], and a photo of multi <i>i-TED</i> detector system.	16
Figure 2.6	Requirements of <i>i-TED</i> and technical solutions.	19
Figure 2.7	Simplified data pipeline for <i>i-TED</i>	20
Figure 3.1	Four <i>i-TED</i> modules placed in front of each other with the target in the middle, allowing for use of both Compton and <i>PET</i> imaging. Image during a study under clinical conditions at the Heidelberg Hadrontherapy Center.	22
Figure 4.1	Normal heatmaps for a given crystal.	28
Figure 4.2	Position artifacts present in the heatmap.	29
Figure 4.3	Anomalous map of reconstructed positions due to clouds for a given crystal.	29
Figure 4.4	General position misreconstruction present in the heatmap.	30
Figure 4.5	Dark zones present in the heatmap.	31
Figure 4.6	Sharp maximums present in the heatmap.	31



Figure 4.7 Distribution of pixel events for each threshold configuration. The green lines represent the mean (dashed) and the median (solid). The outliers correspond to the top and bottom 1% of events. The custom configuration, referred in text as 88c, is labeled with 0. 32

Figure 4.8 Two best configurations for Coincidence Resolving Time (CRT). Measurement taken with i-TED-D and the 511 keV peak of ²²Na in PET mode. . . . 35

Figure 4.9 Time difference (ns) as a function of the difference between the deposited energies in absorber and scatter normalized to the total energy. With the increase of the energy difference between events, the time difference also increases. . . . 35

Figure 4.10 Different phenomena and how they affect timing. From [14, Fig. 17.48-17.50]. 36

Figure 4.11 Drift of the peak in ADC with temperature change for γ -ray energies of 511 keV, 662 keV and 1275 keV. Different integration windows have little impact. 38

Figure 4.12 Correction of the temperature gain change for a ¹³⁷Cs spectrum to different temperatures. 39

Figure 4.13 Uncalibrated spectra of ¹³⁷Cs ins singles mode. 40

Figure 4.14 Counting rate in coincidence mode with ¹³⁷Cs source for difference relative positions between planes. Higher positions correspond to the planes being closer. 41

Figure 5.1 i-TED-E with its full metal casing and without the ⁶Li neutron shield. 43

Figure 5.2 Counting rate in coincidence mode with ¹³⁷Cs source for difference relative positions between planes. Higher positions correspond to the planes being closer. 45


Figure 7.1 Schematic of the back-projection method for a spherical surface. From [43, Fig. 6]. 51

Figure 7.2 Schematic of the definition of the Figure of merit (FoM). 54

Figure 8.1 Setup for the imaging test with ²²Na source in different positions in relation to i-TED-E. 56

Figure 8.2 Imaging results of i-TED-E illustrating the effects of different algorithms, different source positions, and difference focal distances. 57

Figure 8.3 Setup for the imaging test with ²²Na source in different positions in relation to i-TED-A. 58



CSV : GEN-d21c-d2af-ba88-99ce-da2f-70ae-e905-5e92
 DIRECCIÓN DE VALIDACIÓN : <https://portafirmas.redsara.es/pf/valida>
FIRMANTE(1) : BERNARDO BERNARDINO GAMEIRO | FECHA : 09/11/2023 15:40 | NOTAS : F
FIRMANTE(2) : JORGE LERENDEGUI MARCO | FECHA : 09/11/2023 18:46 | NOTAS : CF

Figure 8.4 Selection cuts over three **FOM!** (**FOM!**) related to Compton imaging and their effects on the 511 keV and 1275 keV peaks of ²²Na, positioned differently in relation to **i-TED**. 58

Figure 8.5 59

Figure 8.6 Visualization of the effect of a cut in Angular Resolution Measure (**ARM**) in order to suppress events outside the front position of **i-TED**. Spectra with, without cuts and of the cuts. **ARM** distribution as function of add-back energy. Area under peak in arbitrary units. 60

Figure B.1 Visualization of the effect of a cut in Compton angle in order to suppress events outside the front position of **i-TED**. Spectra with, without cuts and of the cuts. Compton angle distribution as function of add-back energy. Area under peak in arbitrary units. 72


Figure B.2 Complementary imaging results of **i-TED-E** illustrating the effects of different algorithms, different source positions, and difference focal distances. 73

Figure C.1 Calibration interface developed for **i-TED**. 78

Figure C.2 InterSpec calibration interface developed by Sandia National Laboratories (**SNL**). Image from [58]. . . 79

Figure C.3 Data pipeline for **i-TED**. 80

Código seguro de Verificación : GEN-d21c-d2af-ba88-99ce-da2f-70ae-e905-5e92 | Puede verificar la integridad de este documento en la siguiente dirección : <https://portafirmas.redsara.es/pf/valida>



CSV : GEN-d21c-d2af-ba88-99ce-da2f-70ae-e905-5e92
 DIRECCIÓN DE VALIDACIÓN : <https://portafirmas.redsara.es/pf/valida>
FIRMANTE(1) : BERNARDO BERNARDINO GAMEIRO | FECHA : 09/11/2023 15:40 | NOTAS : F
FIRMANTE(2) : JORGE LERENDEGUI MARCO | FECHA : 09/11/2023 18:46 | NOTAS : CF

LIST OF TABLES

Table 4.1	Mean FWHM resolution of the 20 crystals of i-TED (in total and grouped by module) before the beginning of the project and for the initial preliminary characterization. Results obtained for the 662keV peak of Cs137 using a 100ns window and the 888 threshold configuration.	27
Table 4.2	Number of pixels with each threshold configuration. Result obtained with an iterative algorithm to ensure the number of events in the individual pixels was within 5 times the median value for each crystal.	32
Table 4.3	Size of the text file <code>.singles.lmdat</code> in 10^6 Bytes/min for different threshold parameters.	33
Table 4.4	Two best configurations for CRT . Full width at half maximum (FWHM) time resolution in ns for coincidences between 2 crystals of i-TED-D using the two 511 keV γ of ^{22}Na emitted at 180° . . .	34
Table 4.5	Mean resolution at 662 keV for each i-TED using the 888 configuration and 100 ns integration window for comparison with previous results and the 88c configuration and 250 ns integration window for best results, which was the best configuration found.	40
Table 4.6	Mean coincidence resolution at 662 keV for the scatterer with each absorber of i-TED-A using the 88c configuration and 250 ns integration window. The decrease in the resolution labeled "All" is due to different gains in the absorbers.	40
Table 4.7	Alpha activity per second for each crystal of each i-TED with the 88c configuration and a 250 ns integration window.	41
Table 5.1	Mean resolution at 662 keV for each crystal of i-TED-E using the 88c configuration and 200ns integration window and for 511 keV, 1275 keV using a 100ns integration window. The mean resolution of all crystals and all crystals excluding 3 and 4 are included in the last 2 rows.	44



CSV : GEN-d21c-d2af-ba88-99ce-da2f-70ae-e905-5e92


DIRECCIÓN DE VALIDACIÓN : <https://portafirmas.redsara.es/pf/valida>

FIRMANTE(1) : BERNARDO BERNARDINO GAMEIRO | FECHA : 09/11/2023 15:40 | NOTAS : F

FIRMANTE(2) : JORGE LERENDEGUI MARCO | FECHA : 09/11/2023 18:46 | NOTAS : CF

Table 5.2	Mean coincidence resolution at 1275 keV for the scatterer with each absorber of <i>i</i> -TED-E using the 88c configuration and 100 ns integration window. The decrease in the resolution labeled "All" is due to different gains in the absorbers. Measurement conducted at <i>CMAM</i>	45
Table 5.3	Alpha activity per second for each crystal of <i>i</i> -TED-E with the 88c configuration and a 200ns integration window.	46
Table 8.1	Deviation and resolution of the back-projection and analytical algorithms for Compton imaging. Study of ²² Na source in different position and the effect of the focal distance. The last two entries refer to a measurement performed at <i>CMAM</i> with the source at 65 mm of the scatterer. All values in mm.	56
Table B.1	Full results of <i>FWHM</i> time resolution in ns for coincidences between 2 crystals of <i>i</i> -TED-D using the two 511 keV γ -ray of ²² Na emitted at 180°.	71

Código seguro de Verificación : GEN-d21c-d2af-ba88-99ce-da2f-70ae-e905-5e92 | Puede verificar la integridad de este documento en la siguiente dirección : <https://portafirmas.redsara.es/pf/valida>



CSV : GEN-d21c-d2af-ba88-99ce-da2f-70ae-e905-5e92

DIRECCIÓN DE VALIDACIÓN : <https://portafirmas.redsara.es/pf/valida>

FIRMANTE(1) : BERNARDO BERNARDINO GAMEIRO | FECHA : 09/11/2023 15:40 | NOTAS : F

FIRMANTE(2) : JORGE LERENDEGUI MARCO | FECHA : 09/11/2023 18:46 | NOTAS : CF

ACRONYMS

ERC	European Research Council
HYMNS	High-sensitivity Measurements of key stellar Nucleo-Synthesis reactions
CERN	European Organization for Nuclear Research
nToF	Neutron Time-of-Flight facility
ToF	Time-of-Flight
CMAM	Centre for Micro Analysis of Materials
IFIC	Instituto de Física Corpuscular
i-TED	Total-Energy Detector with imaging capability
TED	Total-Energy Detector
GN-Vision	γ & neutron Vision Detector
SiPM	Silicon PhotoMultiplier
ASIC	Application-specific integrated circuit
EMJMD-NucPhys	Erasmus Mundus Joint Master Degree on Nuclear Physics
HISPANoS	Hispalis Neutron Source
CNA	Centro Nacional de Aceleradores
HPGe	High Purity Germanium
PSD	Pulse Shape Discrimination
ACS	Anti-Compton Shield
PMT	PhotoMultiplier Tube
PET	Positron-Electron Tomography
TAC	Total Absorption Calorimeter
APD	Avalanche PhotoDiode
DAQ	Data Acquisition
FWHM	Full width at half maximum
FoM	Figure of merit
ARM	Angular Resolution Measure
MCMC	Markov chain Monte Carlo
MC	Monte Carlo
SNM	Special Nuclear Material
CRT	Coincidence Resolving Time
ML	Machine Learning



CSV : GEN-d21c-d2af-ba88-99ce-da2f-70ae-e905-5e92

DIRECCIÓN DE VALIDACIÓN : <https://portafirmas.redsara.es/pf/valida>

FIRMANTE(1) : BERNARDO BERNARDINO GAMEIRO | FECHA : 09/11/2023 15:40 | NOTAS : F

FIRMANTE(2) : JORGE LERENDEGUI MARCO | FECHA : 09/11/2023 18:46 | NOTAS : CF

HPC High Performance Computing
API Application Programming Interface
SNL Sandia National Laboratories
SOE Stochastic Origin Ensemble
FoV Field of View

Código seguro de Verificación : GEN-d21c-d2af-ba88-99ce-da2f-70ae-e905-5e92 | Puede verificar la integridad de este documento en la siguiente dirección :
<https://portafirmas.redsara.es/pf/valida>



CSV : GEN-d21c-d2af-ba88-99ce-da2f-70ae-e905-5e92

DIRECCIÓN DE VALIDACIÓN : <https://portafirmas.redsara.es/pf/valida>

FIRMANTE(1) : BERNARDO BERNARDINO GAMEIRO | FECHA : 09/11/2023 15:40 | NOTAS : F

FIRMANTE(2) : JORGE LERENDEGUI MARCO | FECHA : 09/11/2023 18:46 | NOTAS : CF

Part I

INTRODUCTION & THEORY

Introduction to the concepts needed to understand the motivation behind the experiment, the functioning of the detector and techniques used. Description of the detection system. Proposed scientific and industrial applications for the detector system.



CSV : GEN-d21c-d2af-ba88-99ce-da2f-70ae-e905-5e92

DIRECCIÓN DE VALIDACIÓN : <https://portafirmas.redsara.es/pf/valida>

FIRMANTE(1) : BERNARDO BERNARDINO GAMEIRO | FECHA : 09/11/2023 15:40 | NOTAS : F

FIRMANTE(2) : JORGE LERENDEGUI MARCO | FECHA : 09/11/2023 18:46 | NOTAS : CF

Código seguro de Verificación : GEN-d21c-d2af-ba88-99ce-da2f-70ae-e905-5e92 | Puede verificar la integridad de este documento en la siguiente dirección :
<https://portafirmas.redsara.es/pf/valida>



CSV : GEN-d21c-d2af-ba88-99ce-da2f-70ae-e905-5e92

DIRECCIÓN DE VALIDACIÓN : <https://portafirmas.redsara.es/pf/valida>

FIRMANTE(1) : BERNARDO BERNARDINO GAMEIRO | FECHA : 09/11/2023 15:40 | NOTAS : F

FIRMANTE(2) : JORGE LERENDEGUI MARCO | FECHA : 09/11/2023 18:46 | NOTAS : CF

INTRODUCTION

The multi *i*-TED detector system was developed within the *HYMNS-ERC* project by the Gamma-ray and Neutron Spectroscopy group of *IFIC*, [1]. The main objective of the *HYMNS-ERC* project is the study of the s-process through neutron capture experiments at *CERN's nToF*, described in [Section 1.1.1](#).

The system was developed to address a common problem of neutron capture (n,γ) cross-section experiments, the relatively high background in the range of energies of interest for nuclear astrophysics (1-100 keV). Incidentally, many of the background events result of neutrons from the beam that are scattered in the target and are captured in the surroundings of the experimental setup and hall, followed by subsequent emission of γ radiation during their decay. The γ radiation background is indistinguishable with common Total-Energy Detector (*TED*), such as those based on C_6D_6 . According to [2, 3], this has been the main source of background in (n,γ) measurements with large neutron scattering to capture cross-section ratio.

To overcome this limitation, an array of Compton cameras was developed in order to select events based on their spacial origin using the imaging capabilities of the detector. The principle behind this type of detector is described in [Section 1.2](#). The detector itself is described in [Chapter 2](#) and characterized in [Chapter 4](#).

1.1 NUCLEAR ASTROPHYSICS

1.1.1 Nucleosynthesis

The question of the relative abundances of the different elements is one of the central topics of Nuclear Astrophysics and the one that birthed the field through the concept of nucleosynthesis in the first half of the XX century, [4, Sect. 1.1]. Nucleosynthesis refers to the different processes through which nuclei are created.

The present thesis concern's itself mainly with stellar nucleosynthesis beyond the iron peak, meaning the creation of nuclei through the nuclear processes that fuel stellar evolution, that closely related to the relative abundance of elements heavier than iron, [4, Sect. 5.6].

The main nuclear capture processes that occur in stellar nucleosynthesis are:



CSV : GEN-d21c-d2af-ba88-99ce-da2f-70ae-e905-5e92

DIRECCIÓN DE VALIDACIÓN : <https://portafirmas.redsara.es/pf/valida>

FIRMANTE(1) : BERNARDO BERNARDINO GAMEIRO | FECHA : 09/11/2023 15:40 | NOTAS : F

FIRMANTE(2) : JORGE LERENDEGUI MARCO | FECHA : 09/11/2023 18:46 | NOTAS : CF

- s-process
- r-process
- p-process

The *i*-TED detector was developed to study the neutron cross-sections of key isotopes along the s-process path.

1.1.2 Neutron capture processes

In contrast with the isotopes up to ^{56}Fe , which were mainly created by fusion, isotopes with higher mass number were formed by neutron capture reactions such as the s- and r-processes, as well as by proton capture processes such as the p-process.

The neutron capture processes are classified based on the relative timescale of the neutron capture and neutron decay by β^- .

When the neutron capture happens slower than the β^- decay, the process is slow (s-process). If otherwise the neutron capture is faster than the β^- decay, the process is rapid (r-process).

- s-process: $\lambda_n \ll \lambda_\beta$
- r-process: $\lambda_n \gg \lambda_\beta$

If the s- or the r-process takes place will depend on the stellar site and the associated neutron flux inside the star. The s-process path, consisting of a chain of neutron capture reactions and beta decays, involves nuclei which are very close to the stability valley. As a consequence, most of them are stable or very long-lived, allowing the direct measurement of the relevant (n,γ) cross section in neutron beam facilities.

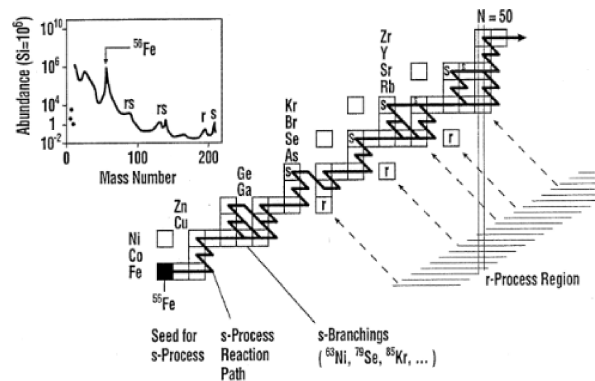


Figure 1.1: Scheme of the neutron-capture processes, including the s-process path, relevant for the motivation of the present work. From [5].



1.1.3 Neutron time-of-flight experiments

A common method for studying the neutron capture cross-section consists in using a pulsed white neutron beam, which covers a large range of energies, combined with the ToF technique.

In a neutron ToF experiment, [4, Sect. 4.6.3], a pulsed proton or electron beam is made to collide with a heavy target in order to generate an intense flux of neutrons which are partially moderated to expand their distribution of kinetic energy. By using the ToF technique, their energy is measured in the experimental hall according to the time they take to travel and react with the sample, located at a well known distance L from the neutron source:

$$E_{k,n} = \frac{1}{2} m_n v_n^2 \quad (1.1)$$

$$= \frac{1}{2} m_n \left(\frac{L}{t_{ToF}} \right)^2 \quad (1.2)$$

With a resolution that improves with the increase of the distance:

$$\frac{\Delta E_{k,n}}{E_{k,n}} = 2 \sqrt{\left(\frac{\Delta L}{L} \right)^2 + \left(\frac{\Delta t_{ToF}}{t_{ToF}} \right)^2} \quad (1.3)$$

The neutrons are then captured by the target isotope of interest and prompt γ -rays originating from the (n,γ) reaction in the sample of interest are detected.

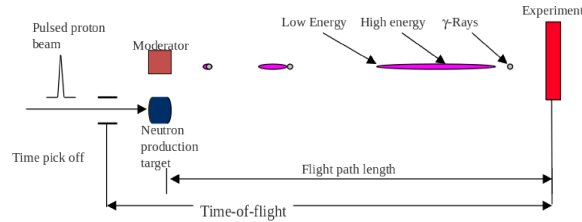


Figure 1.2: Scheme of a neutron time of flight experiment. From [6].

The **HYMNS-ERC** project conducts its experiments in the following neutron ToF facilities:

- nToF, CERN, [7]
- Hispalis Neutron Source (**HISPANoS**), Centro Nacional de Aceleradores (**CNA**), [8]



1.1.3.1 Neutron time of flight experiment

The main experimental facility where the **HYMNS** project is the **nToF** facility at **CERN**. In this facility 20 GeV/c proton pulses are made to collide with a lead spallation target resulting in high energy neutrons. These spallation neutrons are moderated with water in order to widen its distribution into thermal energies. Currently, there are two experimental areas the neutron beam travel to: EAR1 at 185 m (horizontal) [7] and EAR2 at 19 m (vertical) [9], as seen in **Figure 1.3**.

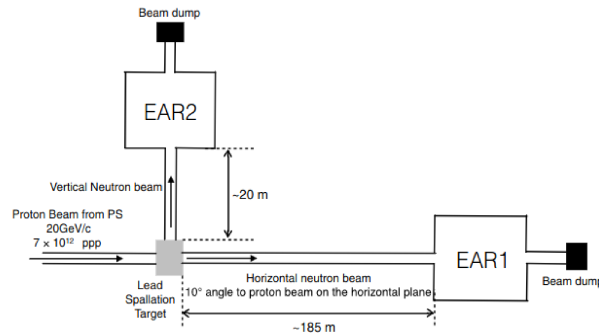


Figure 1.3: **nToF** experiment at **CERN**. From [10].

1.1.4 Challenges

DIRECT NEUTRON BACKGROUND In (n, γ) measurements on isotopes with high neutron flux and high neutron scattering cross-section, orders of magnitude higher than neutron captures, it is important to have detectors with either low neutron sensitivity or ability to discriminate between particles.

NEUTRON-INDUCED γ -RAY BACKGROUND As introduced in **Chapter 1**, for the neutron energies of interest for nuclear astrophysics, most of the background detected is due to γ -rays emitted by surrounding materials, such as the walls or the floor, that capture the scattered neutrons. This background cannot be reduced by low neutron sensitivity as it effectively is γ -ray background. More evolved systems, such as **i-TED**, are required to reduce this background.

COUNTING RATE The development of more intense neutron flux facilities, such as the 20-m flight path **nToF**'s EAR2, reaching $11.5 \times 10^5 \text{ n/cm}^2/\text{pulse}$, poses a challenge in terms of count rate limit of the existing detectors. The high counting rate can become a source of errors due to dead-time and pileup. To overcome this problem, new detectors with higher segmentation have been recently developed [11]. This also discards the possibility of using a neutron and γ detector with par-



ticle discrimination capabilities as it would increase the overall counting rate with the detection of neutrons.

1.2 INTERACTION OF RADIATION WITH MATTER

The *i-TED* detector system is a γ -ray imager based on the Compton imaging technique. To introduce the *i-TED* concept, the interactions between the electromagnetic radiation and the scintillator crystal, resulting in the detection, are described in this section.

1.2.1 Compton scattering

There are three mechanisms of interaction between γ -rays, and electromagnetic radiation in general, and matter: photoelectric effect, Compton scattering and pair production. The probability of interaction by each method depends mainly on the energy of the interacting radiation and the atomic number of the absorber it interacts with. The main interaction method is described in *Figure 1.4*.

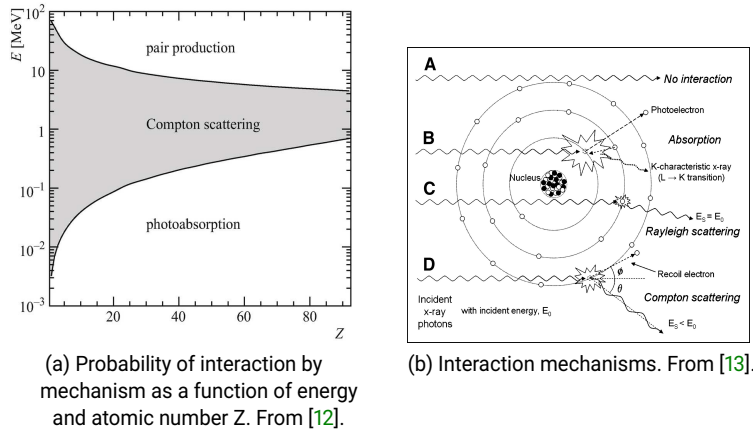


Figure 1.4: Interaction mechanisms of electromagnetic radiation with matter.

As the detector is an array of Compton cameras, the main interaction of interest is Compton scattering. Compton scattering consists of the interaction of electromagnetic radiation with electrons, undergoing elastic scattering and losing energy. The energy of the scattered γ -ray is correlated with the angle of the scattering, θ , by *Equation 1.4*.

$$E'_\gamma = \frac{E_\gamma}{1 + \frac{E_\gamma}{m_e c^2} (1 - \cos \theta)} \tag{1.4}$$

The differential angular cross-section depends on both the atomic number (Z) of the material and the energy of the incoming γ -ray (E_γ), being given by the Klein-Nishina formula:

CSV : GEN-d21c-d2af-ba88-99ce-da2f-70ae-e905-5e92

DIRECCIÓN DE VALIDACIÓN : <https://portafirmas.redsara.es/pf/valida>

FIRMANTE(1) : BERNARDO BERNARDINO GAMEIRO | FECHA : 09/11/2023 15:40 | NOTAS : F

FIRMANTE(2) : JORGE LERENDEGUI MARCO | FECHA : 09/11/2023 18:46 | NOTAS : CF

$$\frac{d\sigma}{d\Omega} = Zr_0^2 \left(\frac{1}{1 + \frac{E_\gamma}{m_0c^2}(1 - \cos\theta)} \right)^2 \left(\frac{1 + \cos^2\theta}{2} \right) \quad (1.5)$$

$$\left(1 + \frac{\left(\frac{E_\gamma}{m_0c^2}\right)^2(1 - \cos\theta)^2}{(1 + \cos^2\theta)\left[1 + \frac{E_\gamma}{m_0c^2}(1 - \cos\theta)\right]} \right) \quad (1.6)$$

This results in a bias towards forward angles for energies greater than 100 keV, as per Figure 1.5.

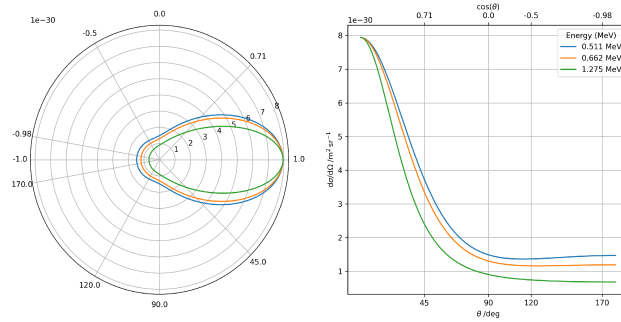


Figure 1.5: Scattering according to the formula of Klein-Nishina for several γ -ray energies that will be used in this work for the characterization of *i*-TED.

1.2.2 Scintillators

One common form of radiation detectors is scintillators. When radiation interacts with the material of a scintillator, it causes atomic and molecular excitation.

There are two kinds of scintillators: organic and inorganic. Although organic scintillators are inexpensive and have a faster response (resolutions of 0.1 ns are achievable), they also have a limited energy resolution, lower light yields and are less dense, resulting in lower efficiency. As such, inorganic scintillators, in particular $\text{LaCl}_3(\text{Ce})$ were used for *i*-TED and are the focus of this section.

Inorganic scintillators function similarly to the band gap model for semiconductor detectors: incident radiation undergoes any of the aforementioned interactions, liberating electrons that excite valence electrons to a higher energy state and the subsequent return to the ground state results in the emission of electromagnetic radiation, usually in or near the visible spectrum, equating to an energy gap of >3 eV.

If the emitted radiation had the same energy as the energy gap, that would result in self-absorption. In order to avoid that effect, and for this process to occur efficiently, dopants are used in order to create



CSV : GEN-d21c-d2af-ba88-99ce-da2f-70ae-e905-5e92

DIRECCIÓN DE VALIDACIÓN : <https://portafirmas.redsara.es/pf/valida>

FIRMANTE(1) : BERNARDO BERNARDINO GAMEIRO | FECHA : 09/11/2023 15:40 | NOTAS : F

FIRMANTE(2) : JORGE LERENDEGUI MARCO | FECHA : 09/11/2023 18:46 | NOTAS : CF

activator states. Those states lay within the band gap and assure that the radiation emitted has lower energy than the energy needed to excite an electron across the band gap.

Another important characteristic of scintillators is the process of decay and light emission. According to the time of decay there are two phenomena: fluorescence and phosphorescence. If the decay is fast to occur ($\approx 10^{-8}s$) there is fluorescence, if the decay is slow to occur ($\approx 10^{-6}s$) there is phosphorescence. As both processes can occur, the decay is expressed by:

$$\frac{dN(t)}{dt} = N_0 \left(\frac{A \times \exp\left(-\frac{t}{\tau_{fast}}\right)}{\tau_{fast}} + \frac{B \times \exp\left(-\frac{t}{\tau_{slow}}\right)}{\tau_{slow}} \right)$$

Where A and B are the constants of decay and depend on both the incident radiation and the scintillator material. Some scintillators present good characteristics that allow the identification of the type of radiation by means of the decay slope, meaning the relation between A and B. This effect is more prevalent in organic scintillators, [14, Sect. 8-I-C-3].



CSV : GEN-d21c-d2af-ba88-99ce-da2f-70ae-e905-5e92

DIRECCIÓN DE VALIDACIÓN : <https://portafirmas.redsara.es/pf/valida>

FIRMANTE(1) : BERNARDO BERNARDINO GAMEIRO | FECHA : 09/11/2023 15:40 | NOTAS : F

FIRMANTE(2) : JORGE LERENDEGUI MARCO | FECHA : 09/11/2023 18:46 | NOTAS : CF

Código seguro de Verificación : GEN-d21c-d2af-ba88-99ce-da2f-70ae-e905-5e92 | Puede verificar la integridad de este documento en la siguiente dirección :
<https://portafirmas.redsara.es/pf/valida>



CSV : GEN-d21c-d2af-ba88-99ce-da2f-70ae-e905-5e92

DIRECCIÓN DE VALIDACIÓN : <https://portafirmas.redsara.es/pf/valida>

FIRMANTE(1) : BERNARDO BERNARDINO GAMEIRO | FECHA : 09/11/2023 15:40 | NOTAS : F

FIRMANTE(2) : JORGE LERENDEGUI MARCO | FECHA : 09/11/2023 18:46 | NOTAS : CF

2.1 TOTAL ENERGY DETECTORS

In neutron capture reactions, a compound nucleus in a highly excited state (above the neutron separation energy) is created, Figure 2.1. In order to determine the neutron capture cross section by means of the ToF technique, one detects the prompt γ -ray cascade emitted in the de-excitation of this nucleus. The main challenge faced lies in the assessment efficiency since it varies with both the energy and the multiplicity.

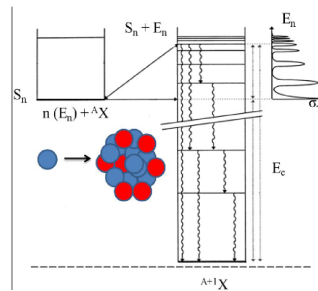


Figure 2.1: Scheme of a neutron capture to an excited state and possible decays to ground state by emission of different γ -ray cascades.

Two types of detectors with very different working principles are used to address this challenge in neutron-capture γ -ray cross section measurements at nToF:

- Total Absorption Calorimeter (TAC)
- TED

With TAC, [15], a high-efficiency 4π detector is used to detect the whole cascade of γ -rays with an efficiency close to 100%. The sum energy and the crystal multiplicity are then used to select events and reject background events.

With TED, [16], instead of measuring the whole γ -ray emission, the objective is to have a detection system that has a low but well-known efficiency which is independent of the cascade pattern. As i-TED is an innovative total energy detector, that is what this work will focus on.

2.1.1 Conditions for the TED technique

LOW-EFFICIENCY If the efficiency to detect each γ -ray $\varepsilon_{\gamma,i} \ll 1$ the $\varepsilon_{\text{cascade}} = 1 - \prod_i (1 - \varepsilon_{\gamma,i}) \approx \sum_i \varepsilon_{\gamma,i}$ approximation is valid.



EFFICIENCY PROPORTIONAL TO γ -RAY ENERGY The efficiency of detection should be proportional to its energy, $\varepsilon_{\gamma,i} \propto E_{\gamma,i}$.

Under this two conditions, the efficiency to detect a cascade proportional to the total energy of the cascade (E_{cascade}) $\varepsilon_{\text{cascade}} \propto \sum_i E_{\gamma,i} = E_{\text{cascade}}$. The cascade energy and independent of the cascade pattern. However, the proportionality between efficiency and energy is not true for many detectors.

2.1.2 Experimental techniques for TED

LOW EFFICIENCY DETECTORS In order to lower the efficiency of each detector, either detectors with low efficiency are used, such as those based on organic scintillators like C_6D_6 , or, if materials with higher efficiency are used, such as the inorganic scintillators of **i-TED**, the low efficiency can be still preserved with an increase in detector segmentation.

PULSE HEIGHT WEIGHTING TECHNIQUE To overcome the non-proportional relation between efficiency and γ -ray energy, a mathematical method has been developed, [16]. A different weight is given depending on the deposited energy so that we can reach the desired proportionality between the efficiency of a cascade and its total energy, verifying **Equation 2.1.2**.

$$\varepsilon_{\text{cascade,weighted}} = \sum_i E_{\gamma,i} = E_{\text{cascade}} \quad (2.1)$$

2.2 EVOLUTION OF GAMMA-RAY SCINTILLATION DETECTORS

According to [17, p. 253], the most important detector properties of modern high-resolution γ -ray spectroscopy are:

- high efficiency for γ -ray
- high energy resolution
- high counting rate
- high probability of full absorption
- high granularity



CSV : GEN-d21c-d2af-ba88-99ce-da2f-70ae-e905-5e92

DIRECCIÓN DE VALIDACIÓN : <https://portafirmas.redsara.es/pf/valida>

FIRMANTE(1) : BERNARDO BERNARDINO GAMEIRO | FECHA : 09/11/2023 15:40 | NOTAS : F

FIRMANTE(2) : JORGE LERENDEGUI MARCO | FECHA : 09/11/2023 18:46 | NOTAS : CF

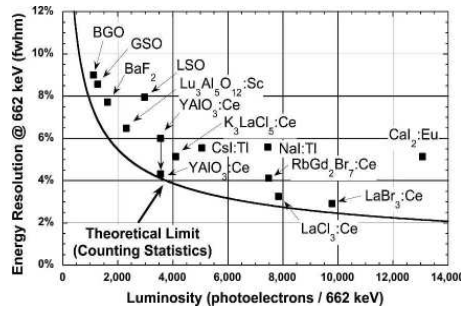


Figure 2.2: Measured energy resolution of several scintillators for 662 keV gamma rays as a function of their light output. From [18].

2.2.1 Materials

With the first two points in mind, new materials have been studied and developed, such as $\text{LaCl}_3(\text{Ce})$ and $\text{LaBr}_3(\text{Ce})$. These, according to [14, p. 251], present several improvements in comparison with previous generations of scintillators:

- high density
- high effective Z
- fast decay times
- high energy resolution
- good wavelength compatibility with photocathodes

Still, they present worse energy resolution than semiconductor-based detectors such as High Purity Germanium (HPGe) ($\approx \times 10$), [19]; more neutron sensitivity than other scintillators such as C_6D_6 or d12-stilbene, [20, 21]; worse timing resolution than organic scintillators; and aren not as suitable for particle discrimination based on Pulse Shape Discrimination (PSD) as CLYC detectors, [22].

2.2.2 Geometries

The geometry of detectors has been developed in order to address the two last points of Section 2.2.

Initially, scintillation detectors consisted only of the detecting material and the light acquisition such as the PhotoMultiplier Tube (PMT), but in order to decrease the Compton continuum a new design was developed: Anti-Compton Shield (ACS), [14, Sect. 10-III-F-1]. This design allows the use of anticoincidence with a secondary detector such as NaI(Tl) or BGO, since in most cases if there are events in coincidence between the main detector and the ACS, then it means the radiation underwent Compton scattering within the main detector.



Following that development, in order to improve the granularity and energy efficiency, segmented detectors were developed, [14, Sect. 20-V-C]. This design allows the use of coincidence and spacial granularity to obtain the original energy of the radiation before scattering by using add back algorithm.

The present project focus on a new generation of detectors: Compton imaging detectors. This type of detector makes use of two planes of detectors, possibly segmented, and of add back algorithms in order to reconstruct the origin of the radiation source. In the case of *i-TED*, this imaging capability has the objective of rejecting events that originate from outside the intended spacial origin of the (n, γ) reaction in *ToF* experiments, which is characterized by high neutron-induced background.

2.3 GAMMA-RAY IMAGING DETECTORS

2.3.1 Compton cameras

A Compton camera, [23, Sect. 2], such as each of the *i-TED* modules, consists of a minimum of two detection planes: the scatterer and the absorber. The incoming γ radiation is expected to undergo one Compton scattering in the scatterer, depositing an energy E_s (or E_1), before depositing its remaining energy, E_a (or E_2), in the second thick detection plane.

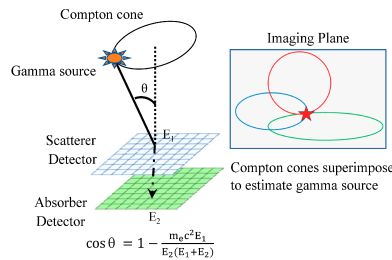


Figure 2.3: Illustration of Compton imaging through overlapping Compton cones. From [24].

By measuring the energy and position of interaction in both planes, and if the add back and initial energies are equal ($E_{\text{add back}} = E_s + E_a = E_\gamma$), it is possible to draw a cone of aperture 2θ , Equation 2.2, that corresponds to the possible origins of the emission of the γ -ray. The intersection of several Compton cones corresponding to the same source of emission will result in the cones overlapping in the position of emission. As such, a good energy and position resolution are fundamental. This is illustrated in Figure 2.3 and animated in [25].



$$\cos \theta = 1 - \left(\frac{m_e c^2 E_s}{E_a E_t} \right) \quad (2.2)$$

2.3.2 PET

When a particle and its antiparticle interact, they annihilate. One example is the e^-e^+ annihilation at low energies that produces two 511keV γ -rays at 180° .

This effect is quite common for β^+ -decays such as the one of ^{22}Na . As the e^-e^+ annihilation emits two γ -rays so well-defined in energies and angular distribution, and as the interaction is so prevalent (β^+ -decays), it is widely used. The fact that the γ -rays are emitted in opposite directions is leveraged to test and validate coincidences between γ detectors.

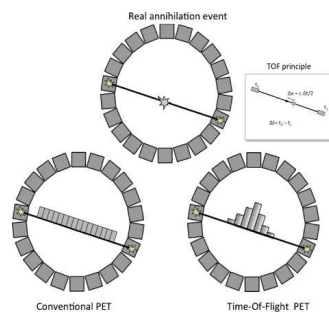


Figure 2.4: Illustration of PET and ToF PET. From [26].

COINCIDENCE TESTING A radioactive β^+ -decay source is placed between both detectors. If the source is equidistant to both detectors, the time difference between the interactions in coincidence should show a peak centered at the origin in time and with a resolution dependent on the sum of the time resolutions of the detectors.

NORMAL PET PET leverages the opposite direction of emission of the two γ -rays. Through extensive geometrical efficiency, it is possible to draw the lines of emission of the γ -rays, which will overlap in the source's position. This effect relies heavily on spacial resolution and is illustrated in Figure 2.4.

TOF PET ToF PET leverages the time coincidence effect and extends it to non-equidistant positions. If the source is closer to one detector than the other, then the γ -ray will be detected before in the detector at closer proximity. This allows the identification of origin of each coincidence measurement as the position on the line is proportional to the



CSV : GEN-d21c-d2af-ba88-99ce-da2f-70ae-e905-5e92

DIRECCIÓN DE VALIDACIÓN : <https://portafirmas.redsara.es/pf/valida>

FIRMANTE(1) : BERNARDO BERNARDINO GAMEIRO | FECHA : 09/11/2023 15:40 | NOTAS : F

FIRMANTE(2) : JORGE LERENDEGUI MARCO | FECHA : 09/11/2023 18:46 | NOTAS : CF

time difference between the measurements. This effect relies heavily on timing resolution and is illustrated in Figure 2.4.

CURRENT STATE-OF-THE-ART PET Nowadays most PET algorithms rely on both methods in order to achieve better resolution PET images.

2.4 THE MULTI I-TED DETECTOR SYSTEM

The multi *i*-TED detector system is composed of 4 Compton cameras, the *i*-TED modules, arranged in a cross, as seen in Figure 2.5. These modules consist, individually, of novel detection systems whose main components have been developed, characterized and optimized in over several years. The reader is referred to [27–31] for all the details.

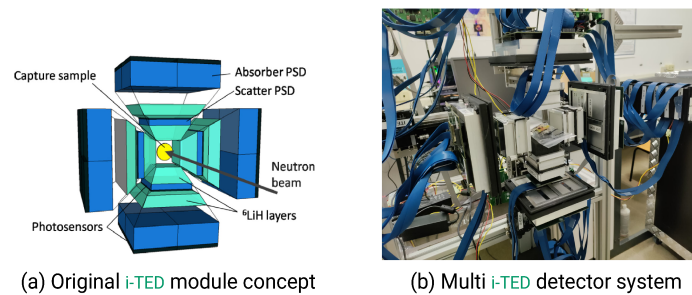


Figure 2.5: The scheme of the original concept, [32], and a photo of multi *i*-TED detector system.

Although the individual *i*-TED modules were operational, only the first demonstrator had been characterized. Moreover, hardware components and processing algorithms had been upgraded. As such, the present work aims to do a final characterization and upgrade of the full array to optimize its performance.

2.4.1 Main components

2.4.1.1 Geometry

The *i*-TED detector system is made of four modules placed in cross, facing the center as shown in Figure 2.5. Each *i*-TED module is made of two parallel planes: the scatterer and the absorber. The scatterer plane is made of a single LaCl_3 crystal with $50 \times 50 \times 15$ mm. The absorber plane is made of four $50 \times 50 \times 25$ mm LaCl_3 crystals centered with the scatterer.

The two planes are connected using the M-683 micropositioning stage from PI-miCos which allow the control of their distance between 10 mm and 60 mm from the back of the scatterer to front of the absorber, [29].



This control over the distance of the planes allows for Dynamic Electronic Collimation, discussed in [29, Sec. 2], which allows a trade-off between efficiency and image resolution, used to accommodate different applications.

2.4.1.2 Detector material

The *i*-TED detector system uses $\text{LaCl}_3(\text{Ce})$ as its scintillator. As previously discussed in Section 2.2.1, LaCl_3 has better characteristics when compared with longer-standing technologies such as $\text{NaI}(\text{Tl})$, including better timing performance, which increases with Cerium dopant, and better energy resolution.

Specifically, $\text{LaCl}_3(\text{Ce})$ was selected instead of $\text{LaBr}_3(\text{Ce})$ due to its lower neutron efficiency, resulting in a small, but necessary for some applications, trade-off for energy resolution.

2.4.1.3 Neutron absorber

In order to further decrease the neutron sensitivity of the *i*-TED detector system, a ^6Li doped polyethylene shield with a thickness of 2 cm was placed in front of the absorber. ^6Li is a moderator of neutrons with a relatively high neutron absorption cross-section, $^6\text{Li}(n, \alpha)^3\text{H}$, and short path for the α particle emitted.

The neutron absorber is placed only in front of the scatterer as it lowers the probability of a neutron coincidence while yielding the desired results with minimal amount of material and cost. Still, current and proposed organic scintillators, such as C_6D_6 and d12-stilbene, have a neutron sensitivity two orders of magnitude lower than $\text{LaCl}_3(\text{Ce})$ with this neutron absorber.

2.4.1.4 Silicon photomultiplier

Silicon PhotoMultiplier (SiPM) are matrices of Avalanche PhotoDiode (APD) operated in Geiger mode and connected in parallel. They collect the radiation, usually in the visible light range, emitted by the decay inside the scintillator. The output signal is obtained from the sum of the individual pixels.

The SiPM in *i*-TED, the ArrayJ-60035-64P-PCB manufactured by SensL, have a surface area of $50 \times 50 \text{ mm}^2$ divided in 8×8 pixels. They are very small when compared to PMTs and their segmented nature allows for the use of algorithms to recover the position of interaction of the original radiation in the scintillator, as per [28, 30, 33].

As they are sensitive to single photons and every generated electron can give origin to the avalanche, they are very sensitive to ambient light input and thermal electrons, respectively. The latter gives rise to the dark rate and is of special consideration.



CSV : GEN-d21c-d2af-ba88-99ce-da2f-70ae-e905-5e92

DIRECCIÓN DE VALIDACIÓN : <https://portafirmas.redsara.es/pf/valida>

FIRMANTE(1) : BERNARDO BERNARDINO GAMEIRO | FECHA : 09/11/2023 15:40 | NOTAS : F

FIRMANTE(2) : JORGE LERENDEGUI MARCO | FECHA : 09/11/2023 18:46 | NOTAS : CF

2.4.1.5 Acquisition system

With such a high number of channels (1280) specialized components are needed for acquisition in coincidence. For our case, PETSys acquisition system, developed for ToF PET providing good characteristics for energy resolution, energy threshold, time resolution, and high number of channels.

PETSYS TOFPET2 ASIC The PETSys ToFPET2 Application-specific integrated circuit (ASIC) is a 64 channel digitizer. The system directly manages the voltage supplied and threshold for each individual pixel.

PETSYS TOFFRONT-END BOARD READOUT This board is responsible for the communication between the Data Acquisition (DAQ) and the ASICs. It receives the data from the ASICs and sends it to the DAQ, allowing up to 72×10^6 events per second and up to 2048 SiPM channels. It is also responsible for setting the configurations for each ASIC and each channel, as well as external clocks and triggers. The latter provides an important capability for measurements in coincidence with other detectors and DAQs and for the use of the system with pulsed beams, such as the case of ToF experiments [31].

PETSYS TOF DATA ACQUISITION BOARD The DAQ board receives the data from optical or copper based SFP+ ports and merges it, sorting by chronological order, and transmitting it to the DAQ computer. It supports up to 250×10^6 events per second.

2.4.2 Requirements and innovative aspects

The i-TED detector was purpose-built for its application to neutron ToF capture cross-section measurements, something noticeable in its design and choice of components, described in this section and illustrated in Figure 2.6.

2.4.2.1 Applicability in neutron capture

Although Compton cameras have been used in medical physics and observational astrophysics (as Compton telescopes), their use in fundamental science, and in beam experiments, is novel, [32]. This has been made possible due to several technological advancements which allowed meeting the requirements discussed in this subsection. Of the requirements discussed below it is worth highlight: energy and position resolution, as well as low neutron sensitivity.



CSV : GEN-d21c-d2af-ba88-99ce-da2f-70ae-e905-5e92

DIRECCIÓN DE VALIDACIÓN : <https://portafirmas.redsara.es/pf/valida>

FIRMANTE(1) : BERNARDO BERNARDINO GAMEIRO | FECHA : 09/11/2023 15:40 | NOTAS : F

FIRMANTE(2) : JORGE LERENDEGUI MARCO | FECHA : 09/11/2023 18:46 | NOTAS : CF

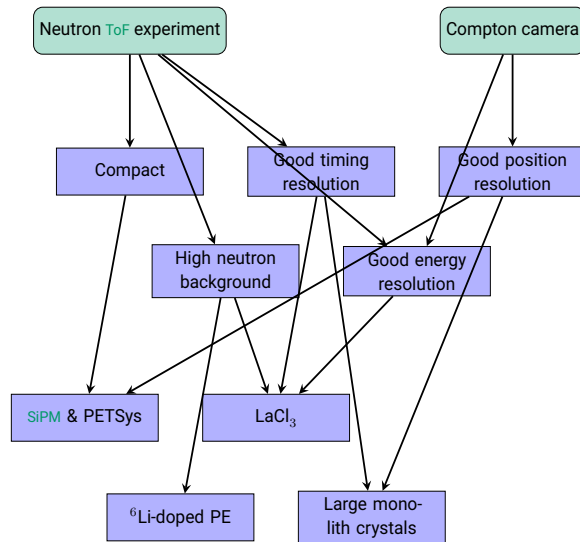


Figure 2.6: Requirements of *i*-TED and technical solutions.

2.4.2.2 Low neutron sensitivity

As discussed in Section 2.4.1.3, ^6Li doped polyethylene was chosen as neutron absorber in order to decrease the neutron sensitivity of the detector taking into account the prevalence of neutron scattering in the targets when compared to the relevant neutron capture, as discussed in Section 1.1.4. To further mitigate this problem, $\text{LaCl}_3(\text{Ce})$ was used as the detector material for its lower neutron sensitivity when compared to other inorganic scintillators, as seen in Section 2.2.1 and Section 2.4.1.2.

2.4.2.3 Position resolution

By using an unsegmented crystal, it is possible to use the algorithms discussed in [28, 30, 33] in order to reconstruct the position of interaction beyond the size of a pixel. This would not be possible with segmented crystals, as per [34].

2.4.2.4 Energy resolution

$\text{LaCl}_3(\text{Ce})$ was chosen as the detector material in order to improve the energy resolution, as discussed in Section 2.2.1 and Section 2.4.1.2. However, the use of SiPMs and segmented photon detectors has a negative impact on the energy resolution. This is evident by the disparity of the value of resolution reported with PETSys and other segmented systems of acquisition when comparing with, for example, PMTs.



2.4.2.5 High number of channels

i-TED has 64 pixels per crystal, 5 crystals per module, and 4 modules, giving a total of 1280 channels that need to be processed in coincidence at the crystal level, at the module level and at the overall detector level. This is made possible by using PETSys' acquisition system.

2.4.2.6 Compactness

For each 64 pixels, there is one PETSys' ASIC with a 14 mm×14 mm chip. The readout, supporting up to 8 ASICs, is 104.5 mm×104.5 mm. This compactness makes the system portable and less prone to interact with the neutrons scattered in neutron capture experiments.

2.4.2.7 Timing resolution

Although organic scintillators have in general better timing resolution than inorganic ones, the current state-of-the-art $\text{LaCl}_3(\text{Ce})$ scintillators can achieve as low as 224 ps resolution, [35]. Nevertheless, to achieve such resolutions an acquisition system with good time resolution has to be used. Although some corrections, discussed in Section 4.2.3.2, can be applied with considerable improvements, the use of large and unsegmented crystals, of SiPMs and of the PETSys acquisition system, which is intended to be used with 511 keV only, result in degradation of this resolution. This is even more accentuated when dealing with a wide range of energies, such as the norm for Compton imaging. Ultimately, this poses a limitation that will be discussed in Section 4.2.3.1.

2.4.3 Data acquisition

Previously, the components responsible for the data acquisition of i-TED were described. Regarding the process of data reduction and pre-processing, it is done through the steps illustrated in Figure 2.7, and described in Section C.3.1.

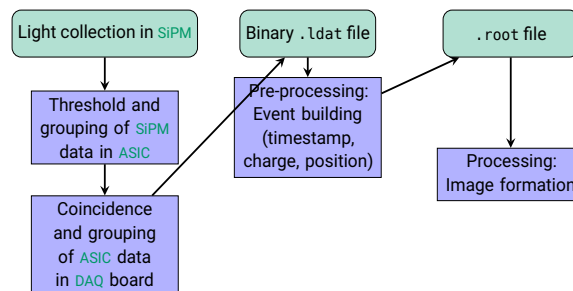


Figure 2.7: Simplified data pipeline for i-TED.



APPLICATIONS OF I-TED

3.1 SCIENTIFIC APPLICATIONS

3.1.1 Neutron capture measurements of astrophysical interest

The main purpose of the **i-TED** detector system is its application to neutron **ToF** capture cross-section measurements of high relevance for nucleo-synthesis studies. As previously discussed in **Chapter 1**, the imaging capabilities of the detector allow for the selection of events based of their spacial origin. This results in an improvement of the peak-to-background ratio, allowing more precise measurements of the neutron capture cross-sections.

The cross-section of neutron captures are of interest for nuclear astrophysics because the abundance of elements in a star, and by extension its evolution, depend on the cross-section of different nuclei that form from it.

There are many cases where more precise measurements are needed in order to explain discrepancies between current theoretical models and the measured relative abundances of elements in the universe, such as $^{79}\text{Se}(n\gamma)$, the first experimental test of **i-TED** [36].

3.2 INDUSTRIAL APPLICATIONS

3.2.1 Range verification in proton therapy

Studies have been conducted into alternatives to conventional radiation therapy, [37], with proton therapy identified as one of the most prominent techniques by virtue of its interaction with matter. Whereas radiation therapy based on γ -rays and electron beams have broad depth-dose distributions in matter, proton radiation is characterized by the Bragg peak, a maximum dose deposition at the end of its trajectory. Evidently, this can be leveraged to deposit most of the dose in the target tumor, minimizing the damage to neighboring tissues. As such, range verification becomes crucial so to minimize inherent range uncertainties associated to anatomical changes, patient setup errors and range errors from uncertainties in particle stopping power, as described by [38].

In order to tackle the fundamental point of range verification in the target tissue, two imaging techniques are being explored: **PET** and **Compton**.



CSV : GEN-d21c-d2af-ba88-99ce-da2f-70ae-e905-5e92

DIRECCIÓN DE VALIDACIÓN : <https://portafirmas.redsara.es/pf/valida>

FIRMANTE(1) : BERNARDO BERNARDINO GAMEIRO | FECHA : 09/11/2023 15:40 | NOTAS : F

FIRMANTE(2) : JORGE LERENDEGUI MARCO | FECHA : 09/11/2023 18:46 | NOTAS : CF

PET imaging, which is well established in the medical field and provides better image resolution, requires the presence of two detectors in front of each other with the source/target in the middle and which depends on the two 511 keV γ -rays from the electron-positron annihilation. Due to the need of two detectors facing each other the field of view is very limited requiring extensive detectors or arrays of detectors. Furthermore, it generally relies on the β^+ -decay of short-lived isotopes between bunches, or longer-lived isotopes detected offline, requiring moving the patient to a dedicated PET scanner.

On the other hand, Compton imaging enables the use of a single detector with a large field of view and the use of any γ -rays which can scatter off of the scatterer and be absorbed by the absorber. This greatly extends the efficiency of the detector since more events can be used both spatially and energy-wise. This also allows the use of prompt γ -rays without the need to move the patient, mitigating biological washout.

Furthermore, since Compton cameras are also γ -ray detectors, if two are positioned in front of each other with the source/target in the middle, as seen in Figure 3.1, both Compton and PET techniques can be used. This fusion of techniques is studied in [38]. Besides range validation, this conjunction can be used for validation and further development of Compton imaging algorithms.



Figure 3.1: Four i-TED modules placed in front of each other with the target in the middle, allowing for use of both Compton and PET imaging. Image during a study under clinical conditions at the Heidelberg Hadrontherapy Center.

3.2.2 Nuclear waste analysis

One increasingly common application for imaging detectors is the analysis of nuclear waste in the dismantling of power plants, [23]. In many cases the nuclear waste, specially that which is highly radioactive, doesn't have the same level of radioactivity throughout the whole material. More commonly, waste classified as having a higher level of radiation is com-



posed of a smaller very radioactive portion and a bigger less radioactive portion, [39].

The use of imaging capabilities allows the identification of more problematic parts of the waste that can be separated, treated and stored according to the respective procedures without treating the whole waste as a monolith. This has significant improvements in terms of storage space and cost of treatment. A proof-of-concept experiment with a single i-TED module has been carried out in Enresa's nuclear storage center, El Cabril, [40].

Imaging capabilities are also of great interest to analyze the activation in nuclear facilities, both industrial and research, that can help improve safety precautions and possible structural damage.



CSV : GEN-d21c-d2af-ba88-99ce-da2f-70ae-e905-5e92

DIRECCIÓN DE VALIDACIÓN : <https://portafirmas.redsara.es/pf/valida>

FIRMANTE(1) : BERNARDO BERNARDINO GAMEIRO | FECHA : 09/11/2023 15:40 | NOTAS : F

FIRMANTE(2) : JORGE LERENDEGUI MARCO | FECHA : 09/11/2023 18:46 | NOTAS : CF

Código seguro de Verificación : GEN-d21c-d2af-ba88-99ce-da2f-70ae-e905-5e92 | Puede verificar la integridad de este documento en la siguiente dirección :
<https://portafirmas.redsara.es/pf/valida>



CSV : GEN-d21c-d2af-ba88-99ce-da2f-70ae-e905-5e92

DIRECCIÓN DE VALIDACIÓN : <https://portafirmas.redsara.es/pf/valida>

FIRMANTE(1) : BERNARDO BERNARDINO GAMEIRO | FECHA : 09/11/2023 15:40 | NOTAS : F

FIRMANTE(2) : JORGE LERENDEGUI MARCO | FECHA : 09/11/2023 18:46 | NOTAS : CF

Part II

DETECTOR UPGRADES AND CHARACTERIZATION

Data-driven upgrades of the multi *i-TED* detector system. In this part, the components and parameters which decreased the system's performance were identified and were either replaced, in case of components, or optimized, in case of the parameters. For the case of parameters, the conditions of use of the system were taken into account since the optimization can depend on the use case. Motivation, mounting and characterization of a new *i-TED* module: *i-TED-E*.



CSV : GEN-d21c-d2af-ba88-99ce-da2f-70ae-e905-5e92

DIRECCIÓN DE VALIDACIÓN : <https://portafirmas.redsara.es/pf/valida>

FIRMANTE(1) : BERNARDO BERNARDINO GAMEIRO | FECHA : 09/11/2023 15:40 | NOTAS : F

FIRMANTE(2) : JORGE LERENDEGUI MARCO | FECHA : 09/11/2023 18:46 | NOTAS : CF

Código seguro de Verificación : GEN-d21c-d2af-ba88-99ce-da2f-70ae-e905-5e92 | Puede verificar la integridad de este documento en la siguiente dirección :
<https://portafirmas.redsara.es/pf/valida>



CSV : GEN-d21c-d2af-ba88-99ce-da2f-70ae-e905-5e92

DIRECCIÓN DE VALIDACIÓN : <https://portafirmas.redsara.es/pf/valida>

FIRMANTE(1) : BERNARDO BERNARDINO GAMEIRO | FECHA : 09/11/2023 15:40 | NOTAS : F

FIRMANTE(2) : JORGE LERENDEGUI MARCO | FECHA : 09/11/2023 18:46 | NOTAS : CF

MULTI *i*-TED DETECTOR SYSTEM

4.1 INITIAL STATUS

The first characterization of an *i*-TED detector, and reference to the present work, was performed after the development of the first module, the so-called *i*-TED demonstrator, and is presented in [29, 41].

After the selection of the components overall characteristics, the development of the full detector array and its installation in the support structure to be used at *n*ToF, the final characterization had not been performed. Moreover, several key features had not been optimized in terms of hardware and software performance.

Upon the start of this thesis project, the *i*-TED detectors had not been used for several months, since the completion of its campaign at the *n*ToF facility of CERN in 2022, [42]. It was also placed on the experimental hall of IFIC, whereas its last characterization took place in the underground facilities of CERN.

The first step in the characterization aimed to confirm the stability of the system with respect to the results obtained in the aforementioned partial characterization. Furthermore, it provided the possibility to study the degradation with time and the difference in conditions (mainly temperature).

A preliminary characterization was performed using a ^{137}Cs source. The energy resolutions obtained are present in Table 4.1, and offer an overview of the stability of the system as well as serving as a starting point into the upgrades described in the next section

<i>i</i> -TED	A	B	C	D	Mean
<i>n</i> ToF 2022/03	7.15 ± 1.13	7.42 ± 0.52	8.56 ± 2.26	6.00 ± 0.28	7.28 ± 1.58
IFIC 2023/02	7.01 ± 1.11	8.45 ± 2.29	7.69 ± 1.48	6.16 ± 0.22	7.33 ± 1.61

Table 4.1: Mean FWHM resolution of the 20 crystals of *i*-TED (in total and grouped by module) before the beginning of the project and for the initial preliminary characterization. Results obtained for the 662keV peak of Cs137 using a 100ns window and the 888 threshold configuration.

4.2 HARDWARE AND SOFTWARE UPGRADES

As introduced in Section 2.4, the multi *i*-TED detector is a complex system consisting of 20 scintillation crystals divided into 4 modules, fea-



CSV : GEN-d21c-d2af-ba88-99ce-da2f-70ae-e905-5e92

DIRECCIÓN DE VALIDACIÓN : <https://portafirmas.redsara.es/pf/valida>

FIRMANTE(1) : BERNARDO BERNARDINO GAMEIRO | FECHA : 09/11/2023 15:40 | NOTAS : F

FIRMANTE(2) : JORGE LERENDEGUI MARCO | FECHA : 09/11/2023 18:46 | NOTAS : CF

turing a total number of 1280 pixels and read-out channels. The combined performance of the scintillation crystals, SiPMs and ASICs, have an influence in the energy resolution, efficiency and reconstruction of the γ -ray interaction positions. All these parameters affect the performance of the Compton modules for the imaging of γ -rays.

With that in mind, the upgrades performed were done so based on complementary measurements that helped identify which component of the system needed upgrade.

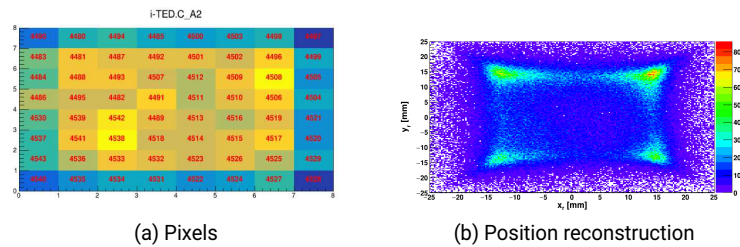
This section will focus on the different problems faced, the identification of its cause and the solutions.

4.2.1 Pixel response and position reconstruction

One way of evaluating the status of the system is by looking at the heatmap of a given scintillator for a given measurement.

There are two types of heatmaps available, counts per pixel and interaction density per position.

For each crystal the two heatmaps are generated, the first based on the cumulative charge fired by each pixel and the second consisting on the reconstructed position of the interaction within the crystal. The algorithm used for the position reconstruction is described in [28, 30]. For reference, Figure 4.1 contains the expected result for each of the heatmaps with proper selection of parameters in order to unwanted effects such as noise. The pin-cushion effect seen in the reconstructed position, that consists in the compression near the edges, is also expected and discussed in [30].



(a) Pixels (b) Position reconstruction

Figure 4.1: Normal heatmaps for a given crystal.

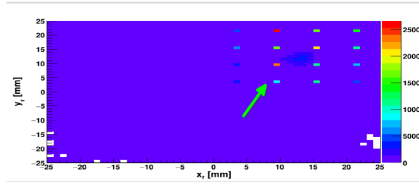
4.2.1.1 Position artifacts

When plotting the heatmaps of the reconstructed positions, the patterns presented in Figure 4.2 were sometimes observed.

The consistency of the position of the patterns over multiple measurements and crystals led those artifacts to be identified as the result of a misfit of the position reconstruction algorithm, influenced by the initial parameters.



This was only present when using the Anger algorithm. By using the Li algorithm instead, the artifacts disappeared. Both algorithms are described in [28].



(a) Pixels

Figure 4.2: Position artifacts present in the heatmap.

4.2.1.2 Localized position misreconstruction

When plotting the heatmaps of the reconstructed positions for each crystal, cases such as Figure 4.3 were observed. This corresponds to a misreconstruction of the interaction position in the crystal in certain zones that spawn the same crystals in all measurements. Those patterns were identified as being caused by the crystals, as changing one crystal with patterns with one without caused them to follow the crystal. This was identified as being caused by "clouds" in the crystal growth, as shown in Figure 4.3. If the cloud was small and far from the window, the patterns were not observed. It was found in 3 crystals.

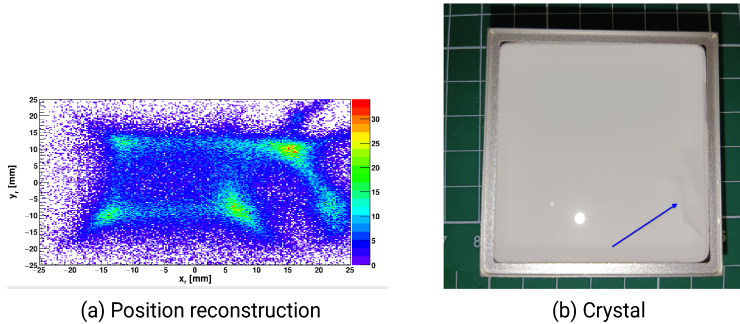


Figure 4.3: Anomalous map of reconstructed positions due to clouds for a given crystal.

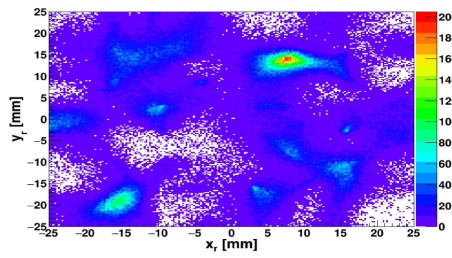
4.2.1.3 General position misreconstruction

In other cases, the position reconstructed presented patterns that weren't localized but that spawn the whole heatmap. This was identified as a mismatch between the physical position of the pixel in the SiPM and its representation in the pixel map, something that has to be checked with the use of every new SiPM.



CSV : GEN-d21c-d2af-ba88-99ce-da2f-70ae-e905-5e92
 DIRECCIÓN DE VALIDACIÓN : <https://portafirmas.redsara.es/pf/valida>
FIRMANTE(1) : BERNARDO BERNARDINO GAMEIRO | FECHA : 09/11/2023 15:40 | NOTAS : F
FIRMANTE(2) : JORGE LERENDEGUI MARCO | FECHA : 09/11/2023 18:46 | NOTAS : CF

This was due to the different possible labels of the pixels in a given SiPM, which corresponds to a factory characteristic. The effect aforementioned can be seen in Figure 4.4.



(a) Position reconstruction

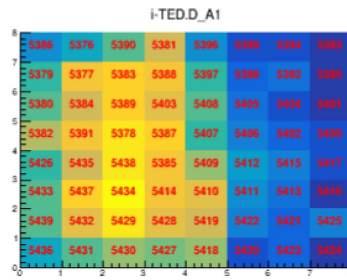
Figure 4.4: General position misreconstruction present in the heatmap.

4.2.1.4 Dark zones

Sometimes it was observed in the heatmaps of both the events and the reconstructed positions that certain regions had considerably lower number of counts. It was noticeable for all measurements whether for background or sources.

Dismounting and remounting the crystals with the same SiPM solved the problem creating more homogeneous heatmaps.

This was identified as being caused by a poor optical coupling of the scintillator to the SiPM. Reapplying optical grease solved the problems. It was noted that, even for grease applied a long time beforehand, uneven pressure applied by the detector casing resulted in the grease flowing out of the areas with higher pressure resulting in a bad optical coupling as evident by Figure 4.5.




(a) Pixels



(b) SiPM

Figure 4.5: Dark zones present in the heatmap.



CSV : GEN-d21c-d2af-ba88-99ce-da2f-70ae-e905-5e92
 DIRECCIÓN DE VALIDACIÓN : <https://portafirmas.redsara.es/pf/valida>
FIRMANTE(1) : BERNARDO BERNARDINO GAMEIRO | FECHA : 09/11/2023 15:40 | NOTAS : F
FIRMANTE(2) : JORGE LERENDEGUI MARCO | FECHA : 09/11/2023 18:46 | NOTAS : CF

4.2.1.5 Multi-pixel sharp maximums

Some pixel heatmaps presented sharp maximums that spawn a few neighboring pixels, even for background measurements. This effect was present mostly near the sides of the casing rather than the center, as shown in Figure 4.6.

Measurements in dark conditions yielded better results and, as such, the problem was identified as light input and solved with black tape or gum near the problematic areas. This was due to fissures in the casing that were not identifiable by sight. The fissures exist due to the thinness of the casing, necessary to minimize the neutron sensitivity for (n,γ) measurements at facilities such as at nToF.

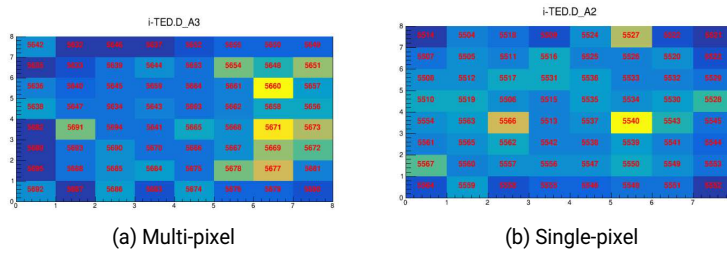



Figure 4.6: Sharp maximums present in the heatmap.

4.2.1.6 Single-pixel sharp maximums

Besides the sharp maximum in neighboring pixels, there were also isolated ones randomly distributed throughout the different crystals, as present in Figure 4.6. By setting higher thresholds for the minimum value of t_E needed to trigger those specific pixels, the maximums disappeared. This problem is addressed in Section 4.2.2. More information on the functioning of the thresholds is given in Section C.3.1.

4.2.2 Pixel threshold optimization

This effect of single-pixel sharp maximums is due to different noise and gain, which can be solved by setting different per-pixel thresholds, since increasing the overall threshold would result in degradation of energy resolution by excluding pulses from good events. To do so, background measurements with different thresholds were performed, and a script was written to iterate over each pixel and based on a given criterion in number of counts, define which pixels had to increase the threshold until those pixels. The criterion was that the 64 individual pixels of each crystal could not have a number of events larger than 5 times the median in a given crystal. The thresholds were set between 7 and 13 in some arbitrary units, obtaining the distribution in Table 4.2.



CSV : GEN-d21c-d2af-ba88-99ce-da2f-70ae-e905-5e92
 DIRECCIÓN DE VALIDACIÓN : <https://portafirmas.redsara.es/pf/valida>
FIRMANTE(1) : BERNARDO BERNARDINO GAMEIRO | FECHA : 09/11/2023 15:40 | NOTAS : F
FIRMANTE(2) : JORGE LERENDEGUI MARCO | FECHA : 09/11/2023 18:46 | NOTAS : CF

Threshold	7	8	9	10	11
Pixels	884	33	258	4	101

Table 4.2: Number of pixels with each threshold configuration. Result obtained with an iterative algorithm to ensure the number of events in the individual pixels was within 5 times the median value for each crystal.

The reference count rate value was calculated for each crystal individually as different crystals can have different count rates related to the different sizes of the scatter and absorber, and the different intrinsic alpha activities. The improvements in homogeneity are better represented by the box plot of Figure 4.7 that shows, for each crystal, the distribution of the number of counts per pixel for various values for the t_E threshold. The last row shows the results with the final customized threshold configuration.

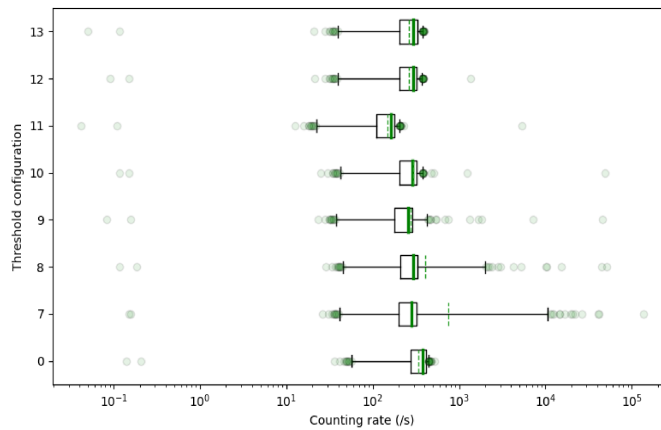


Figure 4.7: Distribution of pixel events for each threshold configuration. The green lines represent the mean (dashed) and the median (solid). The outliers correspond to the top and bottom 1% of events. The custom configuration, referred in text as 88c, is labeled with 0.

Although the results of the optimized configuration, henceforth referred to as 88c, corresponds to a slight improvement in energy resolution when comparing with the 887 threshold, the main improvement observed was the considerable decrease in file size due to a substantial decrease in number of low-energy events, attributable to noise, as shown in Table 4.3. This has obvious benefits in storage, time to process and move files, and, ultimately, price. Previously, such a resolution, although attainable with the 887 threshold, was not used as it had been deemed unpractical due to file size and processing time.



Threshold	6	7	8	9	10	11	Custom
Size (MB/min)	2032	919	496	341	366	173	415

Table 4.3: Size of the text file `.singles.ldat` in 10^6 Bytes/min for different threshold parameters.

4.2.3 Timing

For each crystal of `i-TED`, an event, associated to a γ -ray interaction, is defined by the charge fired in the 64 pixels in a predefined time window that starts with the first pixel firing. Notice that the time window is only defined if the sum of the detections in the pixels is above a threshold. The default method for defining the time of the interaction is by using the timestamp of the first pixel that fired.

4.2.3.1 Timing requirement

As discussed in [Section 2.3.1](#), Compton imaging requires measuring the energy loss by Compton scattering as well as the full energy of the γ -ray. As such, only events in coincidence between the scatter and the absorber are selected. However, it is also required to know the order of the interactions for proper image reconstruction and, by extension, to improve the background rejection capabilities in neutron capture experiments. One way to achieve this goal is to use the time difference, Δt , between the γ -ray interactions in the scatter and absorber planes [31]. With ideal time resolution, one would expect the Δt time distribution to have two peaks associated to the two possible orders of interaction, scatterer \rightarrow absorber and absorber \rightarrow scatterer, the former corresponding to the conditions of interest.

In reality, the finite time resolution broadens the two peaks. In order to distinguish the order of events in the two planes clearly, the distance between the two peaks needs to be greater than the `FWHM` of the Δt distribution. Considering that the resolution is the same regardless of the order of interaction, just in opposite order, the maximum distance of 60 mm between planes and $c \approx 299.8$ mm/ns:

$$FWHM \leq \Delta t \approx \frac{2 \times 60mm}{299.8cm/ns} \approx 400ps \quad (4.1)$$

Meaning a `FWHM` resolution in time of at least 400 ps is needed to be able to distinguish the order of events based solely on time.

4.2.3.2 Optimization for 511 keV

The timing for 511 keV γ -rays was evaluated using the detector in `PET` mode, as discussed in [paragraph 2.3.2](#). It is also worth taking into ac-



CSV : GEN-d21c-d2af-ba88-99ce-da2f-70ae-e905-5e92

DIRECCIÓN DE VALIDACIÓN : <https://portafirmas.redsara.es/pf/valida>

FIRMANTE(1) : BERNARDO BERNARDINO GAMEIRO | FECHA : 09/11/2023 15:40 | NOTAS : F

FIRMANTE(2) : JORGE LERENDEGUI MARCO | FECHA : 09/11/2023 18:46 | NOTAS : CF

count that this is the main purpose the PETSys acquisition system used was developed for.

Following the work of [34, Ch. 3.3], a study of other parameters was performed. For this study, i-TED-D was used with the scatterer and absorber planes at the maximum distance and a ^{22}Na source in the middle of the planes. This source was selected for its emission of two 511 keV γ at 180° characteristic of the electron-positron annihilation, which allowed simultaneous measurements in both planes.

This way, by selecting the coincidences between one scatterer and one absorber, doing energy cuts around the 511 keV peak and plotting the time difference between the events in a coincidence window, a peak centered at 0 was obtained with a standard deviation of twice the time resolution. Deviations from 0 reflected a shift in the position of the source from the central position between the two planes.

From here, the study was carried out using two parameters: the number of pixels taken into account (N_p) to compute the timestamp of the event t_{event} and the weight, calculated as an exponent of the energy measured by the pixel event when calculating the average of the timestamp (W):

$$t_{\text{event}} = \frac{\sum_i^{\min\{N_p, N_t\}} t_{\text{pixel}} \times E_i^W}{\sum_i^{\min\{N_p, N_t\}} E_i^W} \quad (4.2)$$

Two conditions to take into account are that if the number of pixel events to take into account is greater than the total number of pixel events in the interaction ($N_p < N_t$), then all pixel events are used; and if the weight (E_i^W) is small enough that it can't be written in a `C++ long double`, then it is considered 0, meaning that timestamp is not taken into account when calculating the time of the interaction.

The best results obtained for the CRT, which correspond to the images of Figure 4.8, are presented in Table 4.4. The full results are in the appendix, Table B.1.

W	N_p	FWHM (ns)
0	9	2.40
1	25	2.36

Table 4.4: Two best configurations for CRT. FWHM time resolution in ns for coincidences between 2 crystals of i-TED-D using the two 511 keV γ of ^{22}Na emitted at 180° .

Two minimums were identified for $W = 0, N_p = 9$ and $W = 1, N_p = 25$. The configuration $W = 1, N_p = 25$ was taken not only because of having the lowest standard deviation for the peak, but also because it was identified that the distribution of the values is considerably skew to-



wards the central value, whereas for $W = 0, N_p = 9$ there is a presence of more events in the tails of the distribution, as seen in Figure 4.8.

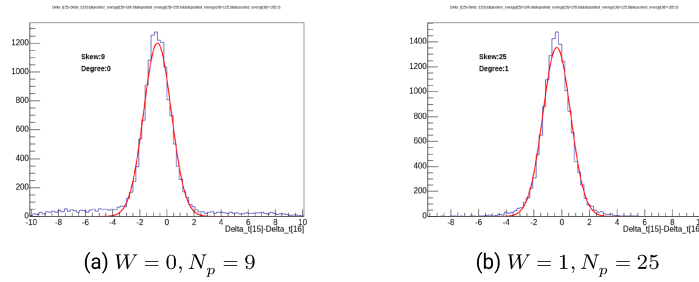


Figure 4.8: Two best configurations for CRT. Measurement taken with i-TED-D and the 511 keV peak of ^{22}Na in PET mode.

4.2.3.3 Dependence on the deposited energy

The optimization discussed previously was carried out for 511 keV γ -rays in PET mode. However, the i-TED detector operating as a Compton camera features very different energy distributions. As such, the behavior of the time was studied for other energies in coincidence, using ^{22}Na and ^{137}Cs , including different energy distributions between the two planes. The results are present in Figure 4.9.

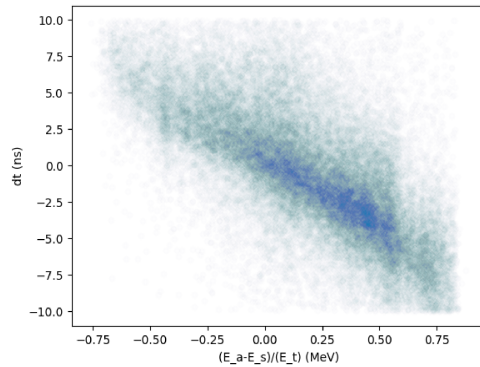


Figure 4.9: Time difference (ns) as a function of the difference between the deposited energies in absorber and scatter normalized to the total energy. With the increase of the energy difference between events, the time difference also increases.

As it can be seen, for the same measurement, the centroid of the time distribution has a dependency on the normalized energy difference. There are different phenomena that can lead to this effect, including:

- Jitter: due to noise, independent of energy.

CSV : GEN-d21c-d2af-ba88-99ce-da2f-70ae-e905-5e92

DIRECCIÓN DE VALIDACIÓN : <https://portafirmas.redsara.es/pf/valida>

FIRMANTE(1) : BERNARDO BERNARDINO GAMEIRO | FECHA : 09/11/2023 15:40 | NOTAS : F

FIRMANTE(2) : JORGE LERENDEGUI MARCO | FECHA : 09/11/2023 18:46 | NOTAS : CF

- Rise time walk: for the same type of radiation, the scintillator used should have the same rise time.
- Amplitude walk: effect aggravated by differences in signal amplitude (which relates to deposited energy), consistent with the results obtained in this work (see Figure 4.9).

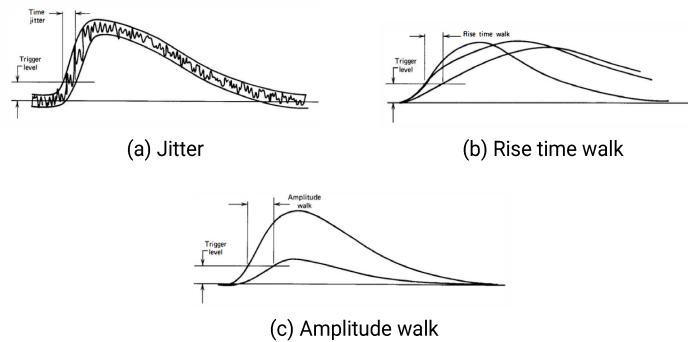


Figure 4.10: Different phenomena and how they affect timing. From [14, Fig. 17.48-17.50].

According to [34, Ch. 1], there are several conditions necessary to obtain optimal CRT. The *i*-TED detector system contains some characteristics that limit its performance:

- **SIPM** instead of **PMT**
 - By using several pixels for a single measurement, uncertainty is introduced
- **Monolith crystals**
 - Segmented crystals with a pixel per segmentation provide better CRT as there is higher light collection in a short amount of time
 - For equal light collection per pixel, monolithic crystals could provide better resolution as the photons travel straight paths
- **Thick crystals**
 - The longer the light travel path, the more CRT deteriorates
- **Temperature**
 - With increase in temperature the gain is lower and the dark counts increase, which increase the effect of jitter

A study using the same acquisition system from PETSys was performed by [34, Ch. 3.4-3.6], using a thinner crystal at a constant temperature of 7°C . This study included several corrections reaching a CRT of 660 ps, about +165% the necessary resolution in order to distinguish the order



of coincidence events in *i-TED* solely based on time for the geometry where the planes are at the maximum possible separation of 60 mm. For the minimum distance of 10 mm the necessary resolution becomes 67 ps, requiring an improvement of one order of magnitude.

4.2.4 Energy resolution

The energy resolution is one of the most important parameters to optimize due to its influence on the uncertainty in the determination of the Compton angle, given in [Equation 2.2](#).

4.2.4.1 Factors to take into account

The energy deposited by each interacting γ -ray is proportional to the light collected by the *SiPM*. As such, it is important to take into account the effects of [Section 4.2.1](#) as well a proper optical coupling to ensure optimal light transference from the crystal to the *SiPM*. The pixel thresholds, previously mentioned and optimized in [??](#), also play a central part as a balance has to be reached between noise (low threshold) and excluding good events (high threshold), since both impact the resolution.

4.2.4.2 ASIC temperature

One of the parameters that most changed the energy resolution was the temperature of the *PETSys ASICs* which integrate the signal of each one of the 64 pixels for each crystal.

The effect of this parameter, although noticeable, was not studied before as the acquisition system was not prepared to include temperature information.

TEMPERATURE Differences in the ambient temperature resulted in noticeable shifts in the *ASIC* gain that lead to a variation in the response to well-known γ -ray energies of calibration sources.

TEMPERATURE CHANGE The change in temperature within a measurement resulted in a shift of the gain, and thus, of the peaks resulting in a perceptibly worse energy resolution.

4.2.4.3 Integration windows

Another parameter that influences the energy resolution of the detector is the time window used to consider an interaction in a given crystal. Currently, an interaction is defined as a time window over all pixels of a given crystal whose energy (in ADC) is above a given threshold.

It is important to take into account that, for very high counting rate, increasing this window may result in including pixel events that correspond to the next interaction in the crystal, resulting in pileup.



CSV : GEN-d21c-d2af-ba88-99ce-da2f-70ae-e905-5e92

DIRECCIÓN DE VALIDACIÓN : <https://portafirmas.redsara.es/pf/valida>

FIRMANTE(1) : BERNARDO BERNARDINO GAMEIRO | FECHA : 09/11/2023 15:40 | NOTAS : F

FIRMANTE(2) : JORGE LERENDEGUI MARCO | FECHA : 09/11/2023 18:46 | NOTAS : CF

In the present project this integration window was kept between 100 and 250 ns. Previously, this window had been fixed at 100 ns, as in [41, Sect. 3.1].

4.2.5 Temperature

As mentioned in Section 4.2.4.2, the temperature of the ASIC influences the gain and, as such, the measured energy.

In order to study this effect and apply a correction to mitigate it, long measurements with ^{22}Na and ^{137}Cs sources were performed. For these measurements, the detector system was not warmed beforehand and the sources had sufficiently high activity in order to have enough statistics at each temperature point of the ASICs increased naturally. This temperature is recorded by the DAQ.

The drift of the peak centroid was plotted as a function of the temperature at which the events were measured. The result is presented in Figure 4.11.

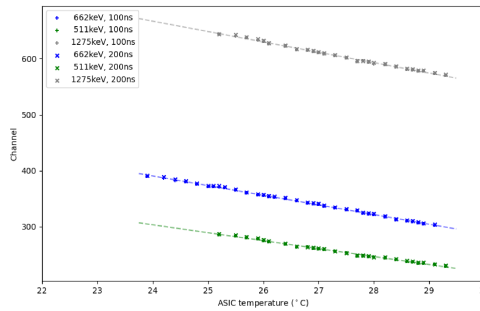


Figure 4.11: Drift of the peak in ADC with temperature change for γ -ray energies of 511 keV, 662 keV and 1275 keV. Different integration windows have little impact.

From here the slope was taken for the measurement of the 662 keV peak if ^{137}Cs , which had the widest range of temperature drift. From the slope, β , the temperature correction was calculated, Equation 4.3. The result of this correction, presented in Figure 4.12, should be done for the ASIC temperature of calibration. However, different calibrations will occur at different temperatures and, even for the same calibration, different ASICs can have different temperatures. Hence, the effects of the correction are shown for different temperatures.



CSV : GEN-d21c-d2af-ba88-99ce-da2f-70ae-e905-5e92

DIRECCIÓN DE VALIDACIÓN : <https://portafirmas.redsara.es/pf/valida>

FIRMANTE(1) : BERNARDO BERNARDINO GAMEIRO | FECHA : 09/11/2023 15:40 | NOTAS : F

FIRMANTE(2) : JORGE LERENDEGUI MARCO | FECHA : 09/11/2023 18:46 | NOTAS : CF

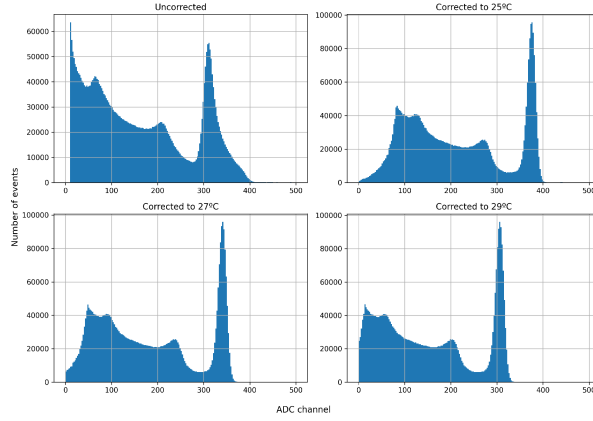


Figure 4.12: Correction of the temperature gain change for a ^{137}Cs spectrum to different temperatures.

$$\beta = \frac{\Delta ADC}{\Delta T} = \frac{ADC_{\text{Measurement}} - ADC_{\text{Reference}}}{T_{\text{Measurement}} - T_{\text{Reference}}} \quad (4.3)$$

$$\Leftrightarrow ADC_{\text{Reference}} = ADC_{\text{Measurement}} + (T_{\text{Reference}} - T_{\text{Measurement}}) \times \beta \quad (4.4)$$

4.3 CHARACTERIZATION

After the upgrades discussed in the previous section, the full characterization of the performance of the final multi *i-TED* detector system was performed.

4.3.1 Energy resolution

Besides the parameters mentioned in Section 4.2.4, the energy resolution depends on the deposited energy.

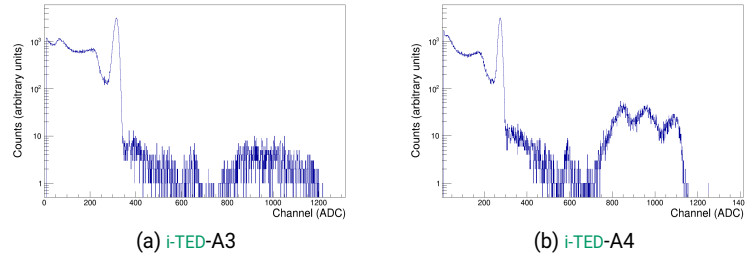
For this section, it was studied for the 662 keV peak of ^{137}Cs , a common benchmark of comparison, visible in Figure 4.13.

4.3.1.1 Singles resolution

The single's resolution is the energy resolution of each of the 5 crystals of each *i-TED*.

The hardware upgrades improved the mean energy resolution from 7.33 ± 1.61 to 7.01 ± 0.79 . The improvement in preprocessing methods, including the per-pixel threshold and integration window, improve it further to 6.71 ± 0.67 , whilst decreasing the noise and, by extension, the file size from 496 MB/min to 415 MB/min.



Figure 4.13: Uncalibrated spectra of ^{137}Cs in singles mode.

i-TED	A	B	C	D	Mean
Comparison	6.58 ± 0.83	7.17 ± 0.18	7.42 ± 1.14	6.87 ± 0.29	7.01 ± 0.79
Best	6.28 ± 0.70	6.90 ± 0.20	6.92 ± 0.90	6.75 ± 0.48	6.71 ± 0.67

Table 4.5: Mean resolution at 662 keV for each i-TED using the 888 configuration and 100 ns integration window for comparison with previous results and the 88c configuration and 250 ns integration window for best results, which was the best configuration found.

4.3.1.2 Resolution in coincidence

The coincidences' resolution is the energy resolution of an i-TED module for the addback energy, this is the sum of the deposited energies of scatterer and absorbers of a given i-TED in coincidence, which is the magnitude used to select events for the Compton imaging. An example of a spectrum in coincidence is present in Figure 8.6.

Absorber	1	2	3	4	Mean	All
Best	8.23 ± 0.38	9.88 ± 0.39	8.49 ± 0.46	8.76 ± 0.62	8.84 ± 0.61	9.62 ± 0.29

Table 4.6: Mean coincidence resolution at 662 keV for the scatterer with each absorber of i-TED-A using the 88c configuration and 250 ns integration window. The decrease in the resolution labeled "All" is due to different gains in the absorbers.

The resolution doesn't change with the distance between planes in most cases. The main effect that could result in a deterioration of energy resolution in coincidence is for γ -rays that suffer scatterings with very small angles as the resolution is worse for low energy depositions.

4.3.2 Counting rate

4.3.2.1 Coincidence

The counting rate for coincidence events with a γ -ray source in front of one i-TED module depends, besides the coincidences coming from



the intrinsic activity, on the proximity between the two planes of *i*-TED, as seen in Figure 4.14.

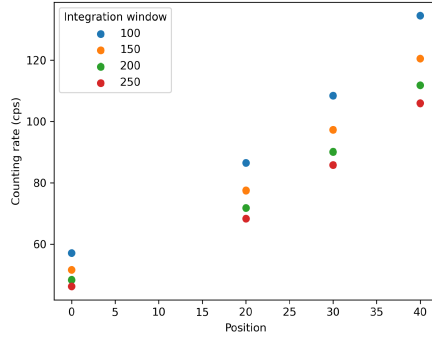


Figure 4.14: Counting rate in coincidence mode with ¹³⁷Cs source for difference relative positions between planes. Higher positions correspond to the planes being closer.

As expected, the counting rate and, as such, the efficiency increase with the proximity of the planes or focal distance. The position is correlated to the distance between the capsules of each plane by Equation 4.3.2.1.

$$\text{Distance} = (75 - \text{Position}) \text{ mm} \tag{4.5}$$

4.3.3 Alpha activity


The alpha activity depends on the growth of the crystal. As it creates a three peak background between 1600 keV and 2800 keV of equivalent electron energy it is better to use crystals with low background, especially if the energies of interest are in that range. This difference is clearly illustrated in Figure 4.13.

<i>i</i> -TED	A	B	C	D
0	24.18± 2.03	143.98±4.91	153.82± 3.29	151.78±4.04
1	157.68± 9.93	124.04±4.10	225.55± 5.97	219.50±6.44
2	117.38± 7.31	204.45±6.34	230.12± 3.28	240.79±4.84
3	36.72± 2.55	221.01±7.23	196.45± 4.85	227.26±6.24
4	222.20±12.55	215.39±7.08	192.53±10.05	231.87±6.15

Table 4.7: Alpha activity per second for each crystal of each *i*-TED with the 88c configuration and a 250 ns integration window.

The values are normalized in time.

CSV : GEN-d21c-d2af-ba88-99ce-da2f-70ae-e905-5e92
 DIRECCIÓN DE VALIDACIÓN : <https://portafirmas.redsara.es/pf/valida>
FIRMANTE(1) : BERNARDO BERNARDINO GAMEIRO | FECHA : 09/11/2023 15:40 | NOTAS : F
FIRMANTE(2) : JORGE LERENDEGUI MARCO | FECHA : 09/11/2023 18:46 | NOTAS : CF



Código seguro de Verificación : GEN-d21c-d2af-ba88-99ce-da2f-70ae-e905-5e92 | Puede verificar la integridad de este documento en la siguiente dirección :
<https://portafirmas.redsara.es/pf/valida>



CSV : GEN-d21c-d2af-ba88-99ce-da2f-70ae-e905-5e92

DIRECCIÓN DE VALIDACIÓN : <https://portafirmas.redsara.es/pf/valida>

FIRMANTE(1) : BERNARDO BERNARDINO GAMEIRO | FECHA : 09/11/2023 15:40 | NOTAS : F

FIRMANTE(2) : JORGE LERENDEGUI MARCO | FECHA : 09/11/2023 18:46 | NOTAS : CF

I-TED-E

5.1 MOTIVATION

With the conclusion of the multi *i*-TED upgrade, characterization and its setup in a configuration that allows its use for both neutron capture experiments and dose monitoring in hadron therapy, the need for an individual *i*-TED detector module arose.

The individual *i*-TED, hereby *i*-TED-E, is to be used in situations that do not warrant the need for multiple Compton cameras, such as for detector testing, or nuclear waste analysis.

Moreover, having a separate *i*-TED allows in the future to perform this kind of experiments without distorting the setup of the multi *i*-TED detector.

This detector was fully built by me as part of my stay at IFIC using spare parts, including components that were new or taken from the multi *i*-TED during the upgrade.

As this detector is not expected to perform in the harsh neutron background conditions of *n*ToF, it has two differences to the other modules. First, it does not include the ${}^6\text{Li}$ shield in front of the scatterer. Second, it has a full metal casing in front of the absorber which facilitates its mounting and a consistent application of pressure over its crystals. This will improve the stability of the optical grease and avoid the dark zones associated to a lack of optical contact described in Section 4.2.1.4. These differences are exhibited in Figure 5.1.

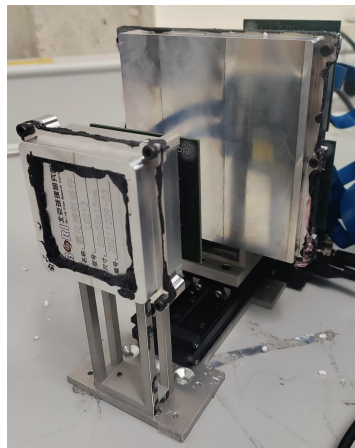


Figure 5.1: *i*-TED-E with its full metal casing and without the ${}^6\text{Li}$ neutron shield.



CSV : GEN-d21c-d2af-ba88-99ce-da2f-70ae-e905-5e92

DIRECCIÓN DE VALIDACIÓN : <https://portafirmas.redsara.es/pf/valida>

FIRMANTE(1) : BERNARDO BERNARDINO GAMEIRO | FECHA : 09/11/2023 15:40 | NOTAS : F

FIRMANTE(2) : JORGE LERENDEGUI MARCO | FECHA : 09/11/2023 18:46 | NOTAS : CF

5.2 CHARACTERIZATION OF I-TED-E

5.2.1 Energy resolution

As the detector has crystals and SiPM that were discarded from the multi i-TED, including those that presented poor energy resolution and "clouds", the performance of i-TED-E is expected to be considerably degraded in comparison with the results presented in Section 4.3. The results presented include the per-pixel threshold optimization described in Section 4.2.2.

5.2.1.1 Singles resolution

A series of 25 runs of 15 s was performed with a ^{137}Cs source. The files were processed with 100 ns and 200 ns coincidence windows to build the response of single crystals and the optimized 88C threshold based of the 887 configuration. An extra measurement with ^{22}Na was conducted at CMAM with 88C threshold and 100 ns.

For the whole detector, i-TED-E presented an overall resolution at the 662 keV ^{137}Cs peak of 8.46 and 8.42 for 100 ns and 200 ns, respectively.

However, this average value hides the considerable discrepancies between crystals presented in Table 5.1.

i-TED-E	662 keV(\pm stat)	511 keV	1275 keV
0	5.79 ± 0.09	7.20	4.26
1	8.41 ± 0.07	8.50	4.74
2	6.99 ± 0.16	9.17	5.47
3	10.55 ± 0.08	9.11	4.36
4	10.37 ± 0.09	13.13	8.65
All	8.42 ± 1.87	9.42	5.50
$\notin\{3\&4\}$	7.06 ± 1.09	8.29	4.82

Table 5.1: Mean resolution at 662 keV for each crystal of i-TED-E using the 88c configuration and 200ns integration window and for 511 keV, 1275 keV using a 100ns integration window. The mean resolution of all crystals and all crystals excluding 3 and 4 are included in the last 2 rows.

This indicates that by changing the components related to absorber 3 and 4 or outright discarding the results from those crystals (which results in a decrease to half of the events) would improve the statistics considerably.



CSV : GEN-d21c-d2af-ba88-99ce-da2f-70ae-e905-5e92

DIRECCIÓN DE VALIDACIÓN : <https://portafirmas.redsara.es/pf/valida>

FIRMANTE(1) : BERNARDO BERNARDINO GAMEIRO | FECHA : 09/11/2023 15:40 | NOTAS : F

FIRMANTE(2) : JORGE LERENDEGUI MARCO | FECHA : 09/11/2023 18:46 | NOTAS : CF

5.2.1.2 Coincidences resolution

Absorber	1	2	3	4	Mean	All
Best	8.20	7.66	8.22	9.67	8.44	8.66

Table 5.2: Mean coincidence resolution at 1275 keV for the scatterer with each absorber of i-TED-E using the 88c configuration and 100 ns integration window. The decrease in the resolution labeled "All" is due to different gains in the absorbers. Measurement conducted at CMAM.

5.2.2 Counting rate

5.2.2.1 Coincidence

Once again, as expected, the counting rate and, as by extension, the efficiency increase with the proximity of the planes. As aforementioned, the position is correlated to the distance between the capsules of each plane by Equation 4.3.2.1.

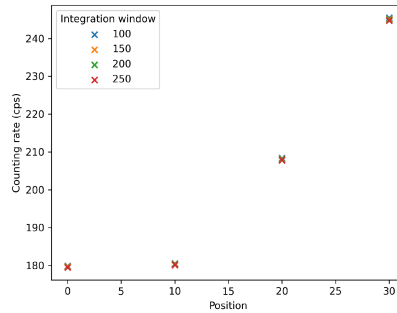



Figure 5.2: Counting rate in coincidence mode with ¹³⁷Cs source for difference relative positions between planes. Higher positions correspond to the planes being closer.

5.2.3 Alpha activity

From the series of 25 runs, the results on Table 5.3 for the alpha activity rate were obtained. The alpha activity rate was calculated as described in Section 4.3.3. As the detector was built from spare crystals, it includes some of the highest and lowest alpha activity rates. The results presented show, once again, the performance variance between crystals.



CSV : GEN-d21c-d2af-ba88-99ce-da2f-70ae-e905-5e92
 DIRECCIÓN DE VALIDACIÓN : <https://portafirmas.redsara.es/pf/valida>
FIRMANTE(1) : BERNARDO BERNARDINO GAMEIRO | FECHA : 09/11/2023 15:40 | NOTAS : F
FIRMANTE(2) : JORGE LERENDEGUI MARCO | FECHA : 09/11/2023 18:46 | NOTAS : CF

i-TED-E	Mean	σ
0	56.33	1.58
1	252.89	3.91
2	13.35	1.03
3	378.62	5.23
4	14.60	1.13

Table 5.3: Alpha activity per second for each crystal of i-TED-E with the 88c configuration and a 200ns integration window.



CSV : GEN-d21c-d2af-ba88-99ce-da2f-70ae-e905-5e92

DIRECCIÓN DE VALIDACIÓN : <https://portafirmas.redsara.es/pf/valida>

FIRMANTE(1) : BERNARDO BERNARDINO GAMEIRO | FECHA : 09/11/2023 15:40 | NOTAS : F

FIRMANTE(2) : JORGE LERENDEGUI MARCO | FECHA : 09/11/2023 18:46 | NOTAS : CF

Part III

IMAGING AND BACKGROUND DISCRIMINATION

Description of different Compton imaging algorithms. Evaluation of the Compton imaging resolution. Analysis of the performance of different **FoM** for background discrimination.



CSV : GEN-d21c-d2af-ba88-99ce-da2f-70ae-e905-5e92

DIRECCIÓN DE VALIDACIÓN : <https://portafirmas.redsara.es/pf/valida>

FIRMANTE(1) : BERNARDO BERNARDINO GAMEIRO | FECHA : 09/11/2023 15:40 | NOTAS : F

FIRMANTE(2) : JORGE LERENDEGUI MARCO | FECHA : 09/11/2023 18:46 | NOTAS : CF

Código seguro de Verificación : GEN-d21c-d2af-ba88-99ce-da2f-70ae-e905-5e92 | Puede verificar la integridad de este documento en la siguiente dirección :
<https://portafirmas.redsara.es/pf/valida>



CSV : GEN-d21c-d2af-ba88-99ce-da2f-70ae-e905-5e92

DIRECCIÓN DE VALIDACIÓN : <https://portafirmas.redsara.es/pf/valida>

FIRMANTE(1) : BERNARDO BERNARDINO GAMEIRO | FECHA : 09/11/2023 15:40 | NOTAS : F

FIRMANTE(2) : JORGE LERENDEGUI MARCO | FECHA : 09/11/2023 18:46 | NOTAS : CF

IMAGING OBJECTIVES OF I-TED

There are two main objectives to be achieved with the imaging capabilities of i-TED.

The objectives are:

- Background Suppression in (n,γ) cross section measurements.
- Source Visualization for imaging applications to medicine or industry.

6.1 BACKGROUND SUPPRESSION

For the main application of i-TED, suppression of background in (n,γ) cross section measurements relevant for the stellar nucleo-synthesis, the imaging capability is second to the background suppression performance.

In (n,γ) cross section measurements carried in ToF experiments the detectors are positioned around the target under study, aiming at an optimum detection efficiency. This results in a simplification into the selection of those events which come from the center of the field of view of the detector instead of an arbitrary position.

Furthermore, some Compton imaging algorithms such as back projection, described in Section 7.1.1, and the analytical, described in Section 7.1.2, the original position of the source is not computed but rather a fit of possible origins. Hence, cuts are not applied on the basis of the origin coordinates but rather on the basis of figures of merit such as the ones discussed in Section 7.2.1 and Section 7.2.2. Nevertheless, imaging reconstruction is important for visualization and validation of the methods.

Moreover, other algorithms such as the Stochastic Origin Ensemble (SOE), discussed in Section 7.1.3, determines the most probable coordinate of the origin of the γ -ray on a per-event basis. In this case, the visualization is key to apply selections in the Cartesian coordinates of the resulting 2D image.

The focus in the application of i-TED for (n,γ) ToF measurements is set on optimizing background suppression to maximize the signal-to-background ratio. For this purpose, several FoM, discussed in Section 7.2, can be used. As they are based on the same magnitudes (energy deposition and position of the interaction in both planes) as the imaging algorithms, an improvement in imaging resolution, this is the uncertainty in the determination of the Compton cone (see Equation 2.2), is correlated with an improvement in the performance of the background



CSV : GEN-d21c-d2af-ba88-99ce-da2f-70ae-e905-5e92

DIRECCIÓN DE VALIDACIÓN : <https://portafirmas.redsara.es/pf/valida>

FIRMANTE(1) : BERNARDO BERNARDINO GAMEIRO | FECHA : 09/11/2023 15:40 | NOTAS : F

FIRMANTE(2) : JORGE LERENDEGUI MARCO | FECHA : 09/11/2023 18:46 | NOTAS : CF

rejection capability. This background suppression is tested with γ -ray sources and the multi i-TED detector, as it is presented in Section 8.2.

6.2 SOURCE VISUALIZATION

In applications such as range verification in hadrontherapy and analysis of nuclear waste, the accurate visualization of the γ -ray sources is the main aim. In these fields, the Compton imaging resolution becomes the main parameter to be optimized.

For hadrontherapy, Compton imaging provides a way of performing range verification, this is visualizing whether the maximum dose (Bragg peak) is deposited inside the target tissue by means of detecting the Prompt gammas. This method avoids the need for detectors facing each other such as with PET imaging.

For nuclear waste analysis, Compton imaging enables imaging, isotopic sorting and activity quantification using a single detector in order to discern between waste with different levels of radioactivity and locate hotspots within one continuous barrel of waste.

In both the aforementioned applications, the main objective is visualization and not background suppression and, as such, the optimization of the imaging capabilities, namely the imaging resolution, is the main objective. The study of imaging resolution with different algorithms is presented in Section 8.1.



CSV : GEN-d21c-d2af-ba88-99ce-da2f-70ae-e905-5e92

DIRECCIÓN DE VALIDACIÓN : <https://portafirmas.redsara.es/pf/valida>

FIRMANTE(1) : BERNARDO BERNARDINO GAMEIRO | FECHA : 09/11/2023 15:40 | NOTAS : F

FIRMANTE(2) : JORGE LERENDEGUI MARCO | FECHA : 09/11/2023 18:46 | NOTAS : CF

COMPTON IMAGING TECHNIQUES

7.1 IMAGING ALGORITHMS

When it comes to imaging using Compton cameras, several methods exist. From those methods, it is necessary to classify them by their output. Some algorithms output the computed position of the origin of the incoming γ -ray whereas others provide probability densities of the possible origin positions.

Although the methods can be extended to three dimensions, the present work focus on the two-dimensional case where the distance between the source and the detector is known and provided as a parameter.

7.1.1 Back-Projection

The simplest method, the back projection, consists in determining the intersection of the Compton cones with a surface of origin of the γ -rays. Usually, the method is implemented with a spherical surface, such as in [43, Sect. IV.A]. However, the present work uses the plane of the source, parallel to both planes of interaction, as the surface to intersect the Compton cone.

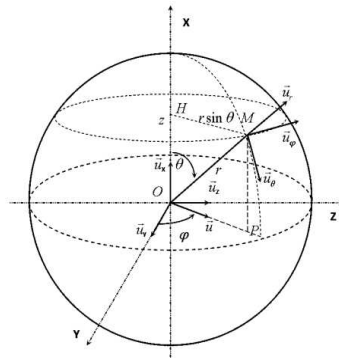


Figure 7.1: Schematic of the back-projection method for a spherical surface. From [43, Fig. 6].

This method does not compute a position for the source on an event-by-event basis, but rather the possible positions defined by the conical generated in the intersection of the Compton cone and the source plane, as seen in Figure 7.2.



CSV : GEN-d21c-d2af-ba88-99ce-da2f-70ae-e905-5e92

DIRECCIÓN DE VALIDACIÓN : <https://portafirmas.redsara.es/pf/valida>

FIRMANTE(1) : BERNARDO BERNARDINO GAMEIRO | FECHA : 09/11/2023 15:40 | NOTAS : F

FIRMANTE(2) : JORGE LERENDEGUI MARCO | FECHA : 09/11/2023 18:46 | NOTAS : CF

7.1.2 Analytical

Another algorithm which provides probability densities of the possible origin positions is the Analytical Algorithm, [44, 45], which uses the analytical inversion of the Compton scattering based on spherical harmonics.

This algorithm requires expensive computations which increase with the degree of the Legendre polynomial used for fitting. As such, the implementation used for *i-TED* uses precomputed values for combinations of energies, angles, and order of Legendre polynomial, saved in table form. This allows significant time-savings. It has also been implemented in GPU with CUDA, allowing a reduction in computing time of ≈ 30 .

7.1.3 Stochastic Ensemble Origin

In contrast with the previous ones, the *SOE* algorithms computes for each incident γ -ray, an emission origin within the plane containing the source.

This method consists of a Markov chain Monte Carlo (*MCMC*) algorithm, commonly coupled to resolution recovery, in order to compute the most probable position of origin for each Compton event.

This method starts from a random position for each event from the back-projection method, computes a density map and then, for each iteration, a new position is selected in the back-projected Compton cone. The new position is used instead of the previous one according to a transition probability.

As the algorithm converges with each iteration, the most probable position of origin for each event is given. As it provides only one position per event instead of a set of probability densities, this method requires more events in order to obtain an image. Hence, it being commonly used with resolution recovery, discussed in [Section 7.1.4](#).

Being an iterative method, it requires considerable resources that increase with the number of entries and the number of iterations. As the back-projection has better performance, and the analytical method has better resolution, the *SOE* has not been studied in the present work.

7.1.4 Resolution Recovery

Resolution recovery is not an imaging algorithm but rather a method of taking into account the different resolutions of the physical quantities



CSV : GEN-d21c-d2af-ba88-99ce-da2f-70ae-e905-5e92

DIRECCIÓN DE VALIDACIÓN : <https://portafirmas.redsara.es/pf/valida>

FIRMANTE(1) : BERNARDO BERNARDINO GAMEIRO | FECHA : 09/11/2023 15:40 | NOTAS : F

FIRMANTE(2) : JORGE LERENDEGUI MARCO | FECHA : 09/11/2023 18:46 | NOTAS : CF

of which they depend on. It can be applied regardless of the imaging method.

This method uses Monte Carlo (MC) in order to sample the uncertainty distributions of the measured energies and interaction positions in both planes. In the current work, this method was implemented using Gaussian distributions, using the measured value as the mean value and the associated uncertainties.

The use of this method allows, through sampling, the increase in statistics while properly reflecting the effect of the finite resolutions and energy and position in the resulting image.

7.2 FIGURES OF MERIT

7.2.1 *Lambda*

In order to explore the reduction in background by means of the Compton imaging capability of i-TED a discrimination analysis has to be made on an event-by-event basis.

To perform this per-event spatial discrimination, the λ FoM [32, Sect. 5], which represents the solution of the Compton scattering formula, describing the intersection of the Compton cone with a plane at the sample center and perpendicular to the circular sample surface (illustrated by the back-projection plane in Figure 7.2), can be employed:

$$\lambda = abs \left[(n_x S_x + n_y S_y + n_z S_z)^2 - \left(1 + \frac{m_{e^-}}{E_T} - \frac{m_{e^-}}{E_A} \right) \times (S_x^2 + S_y^2 + S_z^2) \right] \quad (7.1)$$

Where \vec{n} is the unit vector along the Compton cone and (S_x, S_y, S_z) are the coordinates of interaction in the scatterer plane.

This FoM has units of squared distance and represents the distance from the center of the source. A cut of events with λ smaller than a given value corresponds to events originating within a radius $\sqrt{\lambda}$ of the center in the plane of the source.

7.2.2 *Angular Resolution Measure*

As an alternative to λ , another one-dimensional parameter, the ARM FoM, can be employed for a per-event imaging discrimination. It is defined as the difference between the Compton angle calculated from the positions of interaction assuming the source is in the origin of coordinates and the Compton angle calculated the energies deposited in



CSV : GEN-d21c-d2af-ba88-99ce-da2f-70ae-e905-5e92

DIRECCIÓN DE VALIDACIÓN : <https://portafirmas.redsara.es/pf/valida>

FIRMANTE(1) : BERNARDO BERNARDINO GAMEIRO | FECHA : 09/11/2023 15:40 | NOTAS : F

FIRMANTE(2) : JORGE LERENDEGUI MARCO | FECHA : 09/11/2023 18:46 | NOTAS : CF

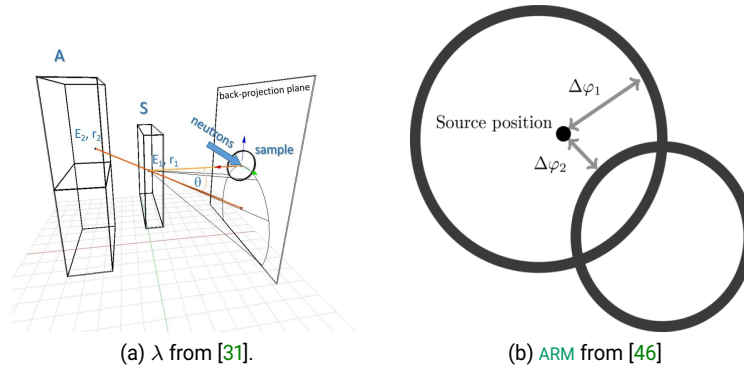


Figure 7.2: Schematic of the definition of the FoM.

both planes using the Compton equation, Equation 1.4, in accordance with [46, Sect. 6] and illustrated in Figure 7.2.

$$ARM = \theta_{\text{Position}} - \theta_{\text{Energy}} \quad (7.2)$$

$$= \arccos \left(\frac{\vec{S} \cdot \vec{A}}{\|\vec{S}\| \|\vec{A}\|} \right) - \arccos \left(1 + \frac{m_{e^-}}{E_T} - \frac{m_{e^-}}{E_A} \right) \quad (7.3)$$

Where S , A are the coordinates of interaction in the scatterer and absorber planes, respectively.

This FoM has units of angle and, for good Compton events, represents the angular difference between the origin of the event and the center.



CSV : GEN-d21c-d2af-ba88-99ce-da2f-70ae-e905-5e92

DIRECCIÓN DE VALIDACIÓN : <https://portafirmas.redsara.es/pf/valida>

FIRMANTE(1) : BERNARDO BERNARDINO GAMEIRO | FECHA : 09/11/2023 15:40 | NOTAS : F

FIRMANTE(2) : JORGE LERENDEGUI MARCO | FECHA : 09/11/2023 18:46 | NOTAS : CF

Taking into account the imaging objectives of the *i-TED* detectors, described in [Chapter 6](#), studies into the background suppression and source visualization were performed. As discussed in [Chapter 3](#), the main application of the multi *i-TED* detector system is background suppression, hence it was used to perform the background suppression tests. On the other hand, in accordance with [Section 5.1](#), *i-TED-E* was not design for neutron *ToF* experiments, but rather for situations such as nuclear waste analysis. As such, it was used for the source visualization tests. Furthermore, an outlook into feature selection and the applicability of *ML* studies is present at the end of the chapter.

8.1 CHARACTERIZATION OF THE IMAGING PERFORMANCE

8.1.1 *Characterization of imaging for i-TED-E*

In accordance with the visualization objective of *i-TED*, [Section 6.2](#), the imaging capabilities of the *i-TED-E* were characterized. With this purpose, two imaging algorithms were used:

- back-projection, [Section 7.1.1](#), for its efficiency and simplicity
- Analytical (with 18 degrees), [Section 7.1.2](#), for its spatial resolution

In this study a ^{22}Na source was placed in a holder at a distance of 90 mm from the front plane of *i-TED-E*, as presented in [Fig. ImagingSetUp](#). The peaks, shown in [Figure 8.2](#), correspond to the source and were fitted with R00T's [\[47\]](#) xygaus in such a way not to take the background into account. As summarized in the results, [Table 8.1](#), it is possible to identify different source positions. As expected, the analytical algorithm, more central source positions, and greater focal distances provide better resolution and position accuracy.

The two Compton imaging algorithms present very distinguishable results. Images generated with the back-projection, have poorer resolution and a more uniform background in comparison with the ones generated by the analytical algorithm, as it is clearly appreciated when comparing panel a and b of [Figure 8.2](#). The former has significantly more background with a narrow peak in the source position. The latter has a very sharp Gaussian in the source position and a significantly enhanced peak-to-background ratio. Some smaller peaks, or artifacts, which appear around the main peak, can be suppressed by setting a lower degree fit, in exchange for position resolution.



CSV : GEN-d21c-d2af-ba88-99ce-da2f-70ae-e905-5e92

DIRECCIÓN DE VALIDACIÓN : <https://portafirmas.redsara.es/pf/valida>

FIRMANTE(1) : BERNARDO BERNARDINO GAMEIRO | FECHA : 09/11/2023 15:40 | NOTAS : F

FIRMANTE(2) : JORGE LERENDEGUI MARCO | FECHA : 09/11/2023 18:46 | NOTAS : CF

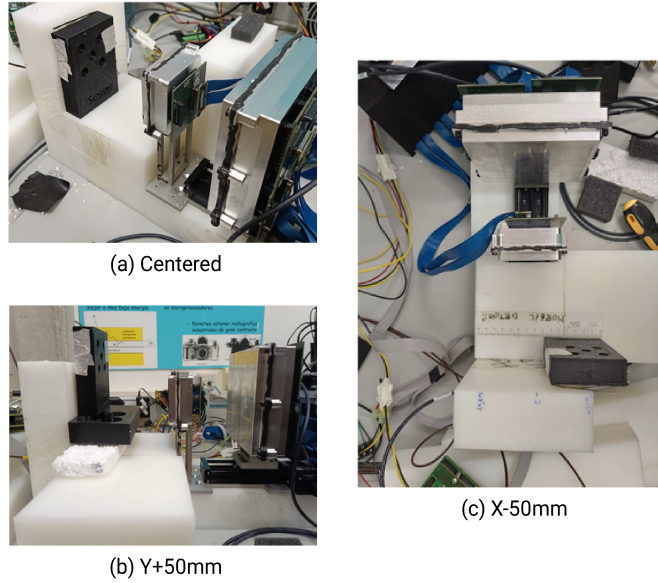


Figure 8.1: Setup for the imaging test with ^{22}Na source in different positions in relation to i-TED-E.

Method	Position	Focal position, Equation 4.3.2.1	X-Centroid	σ_X	Y-Centroid	σ_Y
BP	(-50,0)	10	-36.0	36.2	0.7	37.6
Analytical	(-50,0)	10	-65.3	21.6	3.6	16.0
BP	(0,50)	10	-8.2	17.4	32.7	23.5
Analytical	(0,50)	10	-11.1	14.1	41.8	16.3
BP	(0,0)	10	-6.3	24.0	-0.9	22.8
Analytical	(0,0)	10	-8.9	18.8	0.4	24.0
BP	(0,0)	30	-6.1	27.5	-0.5	28.6
Analytical	(0,0)	30	-10.5	20.1	-0.2	25.3
BP	(0,0)	6	-5.1	15.7	-17.8	17.1

Table 8.1: Deviation and resolution of the back-projection and analytical algorithms for Compton imaging. Study of ^{22}Na source in different position and the effect of the focal distance. The last two entries refer to a measurement performed at CMAM with the source at 65 mm of the scatterer. All values in mm.

8.2 DISCRIMINATION BETWEEN EVENTS IN DIFFERENT POSITIONS

Previously, [31, 48], it had been reported that the λ FoM, Section 7.2.1, provided an effective way of cutting events from the background in order to improve the signal-to-background ratio. In the aforementioned publications, the proof-of-concept of the background rejection capability was based on data and simulations of (n,γ) measurements. The details are out of the scope of this thesis.



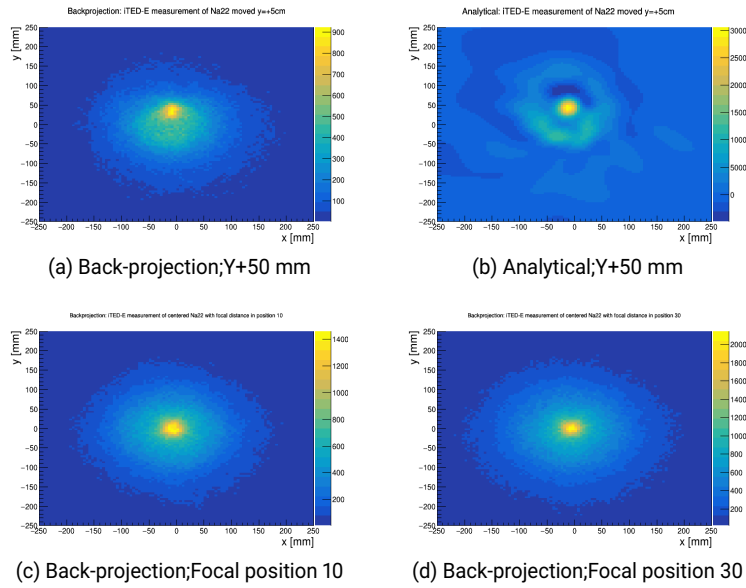


Figure 8.2: Imaging results of i -TED-E illustrating the effects of different algorithms, different source positions, and difference focal distances.

The present study aimed at studying and providing a better understanding of the background rejection in a simpler scenario. In this case, the same γ -ray source was used to emulate both the sample under study located in front of the detector and a background source located elsewhere around detector. Thus, the study described hereafter does not deal with the reduction of the γ background radiation of (n,γ) cross section measurements described in Section 1.1.4, but rather on the discrimination of events from the same decay, thus the same energy, based on the position of origin in relation to i -TED.

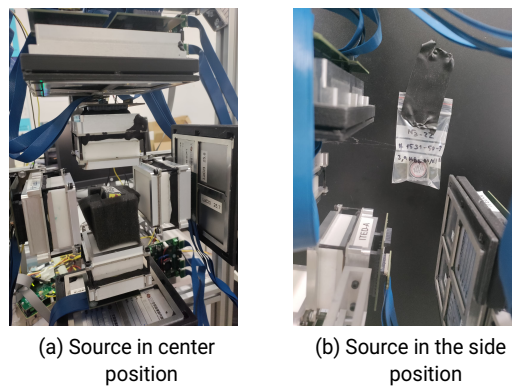
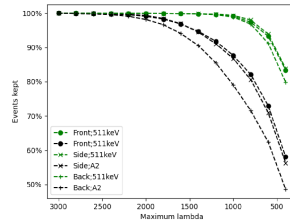


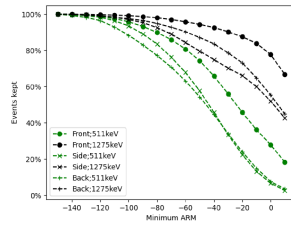
Figure 8.3: Setup for the imaging test with ^{22}Na source in different positions in relation to i -TED-A.



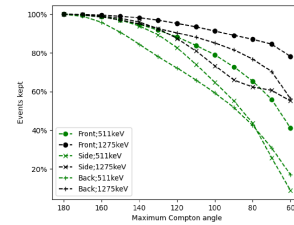
For this purpose, three 900 s measurements of ^{22}Na were performed with the source placed in front of the scatterer, by the side of *i*-TED between the two planes, or behind the absorber, as shown in Figure 8.3. Different FoM were used to make cuts, and the percentage of the number of events in the vicinity of the 511 keV and 1275 keV peaks in relation to the broadest cut are plotted in Figure 8.4. The values of the two peaks are presented separately to show the different behavior with energy. The values were normalized to the broadest but in order to mitigate the effects of the geometric efficiency inherent from placing the source in different positions.



(a) Lambda Section 7.2.1



(b) ARM Section 7.2.2



(c) Compton angle Equation 2.2

Figure 8.4: Selection cuts over three FoM related to Compton imaging and their effects on the 511 keV and 1275 keV peaks of ^{22}Na , positioned differently in relation to *i*-TED.

Clearly, the λ presents similar distributions of the number of events regardless of the position relative to the detector, proving less useful for suppressing radiation from sources than the spatially-extensive and broad-spectrum background of the aforementioned studies, [31, 48]. On the other hand, the ARM and Compton angle show a more accentuated difference based on source positions. This effect is quite visible in Figure 8.6 for the ARM and in Figure B.1 for the Compton angle.

Notice, the results shown in Figure 8.4 were obtained from the integrals of the add-back spectrum including the underlying contribution of ambient background and Compton continuum. To extract the peak contribution, corresponding to the fraction of good Compton events, the peaks were fitted with a Gaussian, while fitting the background with a



second order polynomial. The results using the area of the background subtracted peaks are presented in Figure 8.5.

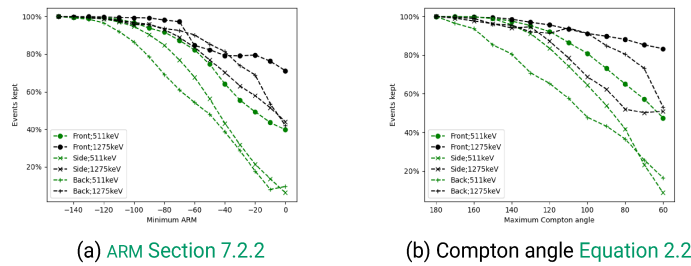


Figure 8.5

It should be noted that by fitting the peaks instead of indiscriminately taking the number of events in the range, the interactions that do not end in full absorptions are effectively removed. In the cases this improves the results, there is indication that γ -rays that escape both planes are affected differently than the events of interest. This can occur in two ways: either by a relative increase in the events of interest, as seen for the 511 keV peak for more restrictive ARM and Compton angle cuts; or by a relative decrease in unwanted events, such as when taking into account the relative decrease in the 1275 keV peak for the measurement of the source in the side of the detector with more restrictive cuts in Compton angle.

8.2.1 Feature selection and outlook for ML studies

As discussed in Appendix C, the importance of computers in physics research can hardly be overstated, and the fast-paced field of ML is no outlier, as argued in [49]. As stated in [50, Chapter 1], the use of ML algorithms thrives with tasks that can formally described, even if too computationally intensive or complex for humans. This, of course, ties nicely into the task at hand, background suppression, having been explored in the context of MC simulations of (n, γ) cross section measurements in neutron ToF experiments, as reported in [31, 48].

8.2.1.1 Model training with simulation and experimental data

The goal of the task is easily described as maximizing the number of good events, according to some metric, whilst minimizing the rest of the events. This metric can be set in a MC simulation as the events originating from the interactions of a γ -ray that is both fully absorbed in the absorber after scattering in the scatterer, and originates from the source. However, with experimental data the situation is not as straight forward. It is not possible to classify events individually as an event



CSV : GEN-d21c-d2af-ba88-99ce-da2f-70ae-e905-5e92

DIRECCIÓN DE VALIDACIÓN : <https://portafirmas.redsara.es/pf/valida>

FIRMANTE(1) : BERNARDO BERNARDINO GAMEIRO | FECHA : 09/11/2023 15:40 | NOTAS : F

FIRMANTE(2) : JORGE LERENDEGUI MARCO | FECHA : 09/11/2023 18:46 | NOTAS : CF

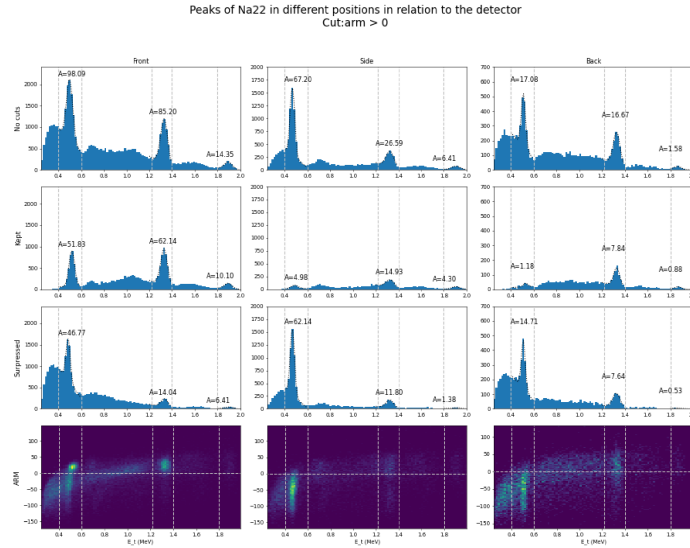


Figure 8.6: Visualization of the effect of a cut in **ARM** in order to suppress events outside the front position of **i-TED**. Spectra with, without cuts and of the cuts. **ARM** distribution as function of add-back energy. Area under peak in arbitrary units.

with seemingly the expected energy depositions and interactions can have been originated in the background or be a higher energy γ -ray from the source that is not fully absorbed. This leads to one of the fundamental principles of **ML**: data quality. Data quality encompasses several characteristics such as completeness, validity and consistency, yet, most relevant to the current problem, it includes accuracy. The inclusion of unwanted events in the training data, commonly referred as data leakage, hinders the accuracy of the data and, by extension, the quality of the model. A scoring algorithm could be designed in order to mitigate the issue, relying on statistical properties rather than single entries, but ideally a study should be conducted based on synthetic data from **MC** simulation.

8.2.1.2 Feature selection for Machine Learning

Regarding the complexity that warrants the use of **ML** algorithms instead of analytical ones, although the good events can intuitively be described, their description is not as straight forward in terms of their properties. An event can be described by a high number of dimensions: eight from measurements (position and energy in each plane), plus the time difference of interaction; three **FoM** (with capabilities in restricting unwanted events, as established in [Section 8.2](#)), plus the cross section of the Compton scattering (calculated from the Klein-Nishina, [Equation 1.6](#), which provides information about the underlying physics, and possibly provide better models in accordance with [51]). This results



in 13 dimensions over which data can possibly be correlated and used to select events. Luckily, as stated in [50, Chapter 1], optimization over a high number of dimensions, too complex for human pattern recognition, is one case where ML algorithms triumph.

8.2.1.3 Machine Learning outlook

In conclusion, a study into the applicability of ML algorithms for background suppression with i-TED should be performed using MC simulations of point-like in different spacial distributions to expand on the work of [31, 48] and to better understand the response of the detector and the importance of each feature in suppressing events (feature selection).



CSV : GEN-d21c-d2af-ba88-99ce-da2f-70ae-e905-5e92

DIRECCIÓN DE VALIDACIÓN : <https://portafirmas.redsara.es/pf/valida>

FIRMANTE(1) : BERNARDO BERNARDINO GAMEIRO | FECHA : 09/11/2023 15:40 | NOTAS : F

FIRMANTE(2) : JORGE LERENDEGUI MARCO | FECHA : 09/11/2023 18:46 | NOTAS : CF

Código seguro de Verificación : GEN-d21c-d2af-ba88-99ce-da2f-70ae-e905-5e92 | Puede verificar la integridad de este documento en la siguiente dirección :
<https://portafirmas.redsara.es/pf/valida>



CSV : GEN-d21c-d2af-ba88-99ce-da2f-70ae-e905-5e92

DIRECCIÓN DE VALIDACIÓN : <https://portafirmas.redsara.es/pf/valida>

FIRMANTE(1) : BERNARDO BERNARDINO GAMEIRO | FECHA : 09/11/2023 15:40 | NOTAS : F

FIRMANTE(2) : JORGE LERENDEGUI MARCO | FECHA : 09/11/2023 18:46 | NOTAS : CF

Part IV

CONCLUSION

Summary of the results achieved in this thesis project.



CSV : GEN-d21c-d2af-ba88-99ce-da2f-70ae-e905-5e92

DIRECCIÓN DE VALIDACIÓN : <https://portafirmas.redsara.es/pf/valida>

FIRMANTE(1) : BERNARDO BERNARDINO GAMEIRO | FECHA : 09/11/2023 15:40 | NOTAS : F

FIRMANTE(2) : JORGE LERENDEGUI MARCO | FECHA : 09/11/2023 18:46 | NOTAS : CF

Código seguro de Verificación : GEN-d21c-d2af-ba88-99ce-da2f-70ae-e905-5e92 | Puede verificar la integridad de este documento en la siguiente dirección :
<https://portafirmas.redsara.es/pf/valida>



CSV : GEN-d21c-d2af-ba88-99ce-da2f-70ae-e905-5e92

DIRECCIÓN DE VALIDACIÓN : <https://portafirmas.redsara.es/pf/valida>

FIRMANTE(1) : BERNARDO BERNARDINO GAMEIRO | FECHA : 09/11/2023 15:40 | NOTAS : F

FIRMANTE(2) : JORGE LERENDEGUI MARCO | FECHA : 09/11/2023 18:46 | NOTAS : CF

SUMMARY

As previously stated, the work carried out for the current thesis project was divided in two parts: the upgrade and characterization of *i*-TED detectors; and imaging studies. The most prominent results are summarized and discussed below.

9.1 DETECTOR UPGRADES AND CHARACTERIZATION

9.1.1 *Starting point and upgrades*

Upon the start of the project multi *i*-TED had been mounted but not characterized, nor upgraded, nor optimized. During its upgrade, six types of anomalous functioning were identified and documented, [Section 4.2.1](#), so that they can be more easily spotted and corrected. In order to solve this issues, several upgrades were performed in the first part of this work, including changing several components of the detectors, selection of more stable algorithms, and the development of a program to individually optimize the threshold of SiPM's pixels. Comparing to the initial measurements done with the 888 threshold, the change also led to a $\approx 16\%$ reduction of the raw file size, while improving energy resolution by $\approx 8\%$, and decreasing the noise.

The timing performance was initially studied for PET mode, using the two 511 keV emitted from ^{22}Na 's decay. A method proposed in the literature was implemented, with a wider range for the parameters, resulting in a $\approx 30\%$ improvement in timing resolution. A second study was conducted with a broader range of energies in Compton mode, leading to the identification of possible signal processing issues that where found to deteriorate this resolution. It was concluded that technological developments in scintillators and SiPMs are needed in order to determinate the order of γ -ray interactions between planes based on timestamp. All the codes used for the data-driven upgrades were fully developed as part of this project.

Lastly, a study into the effect of the ASIC temperature was conducted, and a correction was implemented to counter the $\approx -15\text{ADC}/^\circ\text{C}$ drift. Regarding the multi *i*-TED detector system, comparing the initial conditions with the upgrades to the hardware and optimization of methods, an improvement of $\approx 8\%$ in singles resolution was achieved, along with a mean coincidence resolution between crystals of 8.84 ± 0.61 , both results at 662 keV. The counting rate in coincidence mode and alpha activity were also mapped. This was the first full characterization of the detector.



CSV : GEN-d21c-d2af-ba88-99ce-da2f-70ae-e905-5e92

DIRECCIÓN DE VALIDACIÓN : <https://portafirmas.redsara.es/pf/valida>

FIRMANTE(1) : BERNARDO BERNARDINO GAMEIRO | FECHA : 09/11/2023 15:40 | NOTAS : F

FIRMANTE(2) : JORGE LERENDEGUI MARCO | FECHA : 09/11/2023 18:46 | NOTAS : CF

9.1.2 *i*-TED-E

A new *i*-TED detector was mounted from the (best) extra components of the upgrades of the multi *i*-TED. This is of great interest to the HYMNS research group, specially for field applications. It was also fully characterized, with a mean resolution in singles of 8.42 ± 1.87 and in coincidence of 8.44 ± 0.75 , as they were built of spare parts.

9.2 IMAGING STUDIES

9.2.1 *Characterization of the imaging performance*

The Compton imaging performance is the key feature for applications of the *i*-TED detector to hadrontherapy and industry. Moreover, reconstructing accurate Compton images serves as performance validation for its main scientific aim: rejecting background events in (n, γ) ToF experiments. With that in mind, two of the main algorithms for Compton imaging were used and characterized for sources in and out of the center of the Field of View (FoV).

9.2.2 *Discrimination between events in different positions*

The main aim of *i*-TED is the application of selections in the Compton imaging domain to improve the signal-to-background ratio in (n, γ) ToF measurements. The goal is to enhance events coming from a sample under study located in front of the detector, while suppressing all the γ -rays spatially originating elsewhere in the experimental area. To study this capability, in this work measurements were performed with the same source in different positions in relation to one of the *i*-TED modules in order to better understand the different behaviors of the FoM. The Compton angle and the ARM were identified as the best dimensions to perform cuts in order to suppress events originated from outside the target position (front of the detector). A ML study is proposed and motivated in order to expand previous work with the results obtained in this thesis.



CSV : GEN-d21c-d2af-ba88-99ce-da2f-70ae-e905-5e92

DIRECCIÓN DE VALIDACIÓN : <https://portafirmas.redsara.es/pf/valida>

FIRMANTE(1) : BERNARDO BERNARDINO GAMEIRO | FECHA : 09/11/2023 15:40 | NOTAS : F

FIRMANTE(2) : JORGE LERENDEGUI MARCO | FECHA : 09/11/2023 18:46 | NOTAS : CF

Código seguro de Verificación : GEN-d21c-d2af-ba88-99ce-da2f-70ae-e905-5e92 | Puede verificar la integridad de este documento en la siguiente dirección :
<https://portafirmas.redsara.es/pf/valida>

Part V

APPENDIX



CSV : GEN-d21c-d2af-ba88-99ce-da2f-70ae-e905-5e92

DIRECCIÓN DE VALIDACIÓN : <https://portafirmas.redsara.es/pf/valida>

FIRMANTE(1) : BERNARDO BERNARDINO GAMEIRO | FECHA : 09/11/2023 15:40 | NOTAS : F

FIRMANTE(2) : JORGE LERENDEGUI MARCO | FECHA : 09/11/2023 18:46 | NOTAS : CF

Código seguro de Verificación : GEN-d21c-d2af-ba88-99ce-da2f-70ae-e905-5e92 | Puede verificar la integridad de este documento en la siguiente dirección :
<https://portafirmas.redsara.es/pf/valida>



CSV : GEN-d21c-d2af-ba88-99ce-da2f-70ae-e905-5e92

DIRECCIÓN DE VALIDACIÓN : <https://portafirmas.redsara.es/pf/valida>

FIRMANTE(1) : BERNARDO BERNARDINO GAMEIRO | FECHA : 09/11/2023 15:40 | NOTAS : F

FIRMANTE(2) : JORGE LERENDEGUI MARCO | FECHA : 09/11/2023 18:46 | NOTAS : CF

FUTURE DEVELOPMENTS BASED ON THE I-TED CONCEPT

A.1 GN-VISION

For the industrial applications of *i-TED*, there is a growing need for the ability to combine neutron and γ -ray imaging. This need is enhanced by new hadrontherapy techniques such as Neutron Capture Therapy, and the need to identify fissioning nuclei and Special Nuclear Material (SNM) for Nuclear Inspections and Proliferation purposes.

As such, γ & neutron Vision Detector (GN-Vision), a variation of *i-TED*, is currently being developed with a CLYC scintillator in the scatterer plane and a pinhole collimator instead of neutron shield. The CLYC allows particle discrimination to be performed based on a FoM associated to the pulse shape, due to the different decay time of the neutron and γ -ray signals. The pinhole allows for pinhole imaging of neutrons which would be coupled to Compton imaging for γ -rays.

A.1.1 Applicability for neutron captures of astrophysical interest

It could be asked why not use GN-Vision instead of *i-TED* for neutron captures of astrophysical interest since it can discriminate particles and, as such, discard neutrons in order to keep only γ -ray events. While this would be feasible, in practice the high rate of neutrons scattered, instead of captured, by the target in neutron captures experiments would result in a decrease of γ -ray efficiency due to the dead-time and pileup, as discussed in Section 1.1.4, which arises from the slow signals ($\approx \mu s$) of CLYC crystals.

A.2 I-TED WITH ANTI-COMPTON SHIELD

In coincidence mode, events from the background and events from sources in other positions can be suppressed, as per [14, Sect. 10-III-F-1] and Chapter 8, respectively. The remaining events are random coincidences and, mostly, γ -rays that suffer Compton scattering in both planes.

One possible way of suppressing γ -rays that are not absorbed in the absorber plane is the inclusion of another scintillator to work as an ACS. With the inclusion of this scintillator, which should maximize the



CSV : GEN-d21c-d2af-ba88-99ce-da2f-70ae-e905-5e92

DIRECCIÓN DE VALIDACIÓN : <https://portafirmas.redsara.es/pf/valida>

FIRMANTE(1) : BERNARDO BERNARDINO GAMEIRO | FECHA : 09/11/2023 15:40 | NOTAS : F

FIRMANTE(2) : JORGE LERENDEGUI MARCO | FECHA : 09/11/2023 18:46 | NOTAS : CF

cross-section with γ -rays, events can be discarded in case of three coincidences as it would correspond to events that escape the absorber. This scintillator doesn't have requirements in position resolution, can be made to only take one channel, and, unless it doubles as a way to recover those events, there isn't a requirement in energy resolution.

The material and geometry of such a component would warrant another study in order to maximize its efficiency and limit its neutron sensitivity.



CSV : GEN-d21c-d2af-ba88-99ce-da2f-70ae-e905-5e92

DIRECCIÓN DE VALIDACIÓN : <https://portafirmas.redsara.es/pf/valida>

FIRMANTE(1) : BERNARDO BERNARDINO GAMEIRO | FECHA : 09/11/2023 15:40 | NOTAS : F

FIRMANTE(2) : JORGE LERENDEGUI MARCO | FECHA : 09/11/2023 18:46 | NOTAS : CF

COMPLEMENTARY MATERIAL OF THE CHARACTERIZATION

B.1 DETECTOR UPGRADES AND CHARACTERIZATION

	1	2	3	4	5	6	7	8	9	10
0	3.44	3.19	3.03	2.90	2.75	2.62	2.51	2.43	2.40	2.40
1	3.44	3.41	3.38	3.34	3.29	3.24	3.16	3.10	3.03	2.95
2	3.44	3.59	3.49	3.47	3.44	3.44	3.45	3.48	3.51	3.53
3	3.44	3.53	3.50	3.51	3.54	3.63	3.72	3.83	3.93	4.05
	11	12	13	14	15	16	17	18	19	20
0	2.43	2.50	2.59	2.71	2.87	3.02	3.18	3.35	3.49	3.63
1	2.88	2.81	2.75	2.70	2.64	2.59	2.54	2.51	2.47	2.44
2	3.58	3.62	3.65	3.70	3.73	3.77	3.80	3.84	3.88	3.92
3	4.14	4.27	4.38	4.48	4.58	4.69	4.78	4.87	4.98	5.10
	21	22	23	24	25	-	-	-	-	-
0	3.76	3.89	3.97	4.07	4.18					
1	2.42	2.40	2.38	2.36	2.36					
2	3.94	3.97	4.02	4.05	4.07					
3	5.20	5.31	5.39	5.49	5.58					

Table B.1: Full results of **FWHM** time resolution in ns for coincidences between 2 crystals of **i-TED-D** using the two 511 keV γ -ray of ^{22}Na emitted at 180° .



B.2 IMAGING AND BACKGROUND DISCRIMINATION

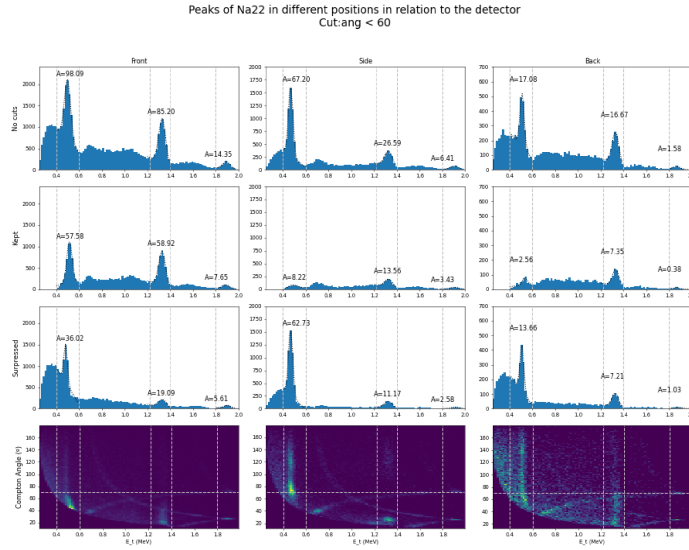


Figure B.1: Visualization of the effect of a cut in Compton angle in order to suppress events outside the front position of *i*-TED. Spectra with, without cuts and of the cuts. Compton angle distribution as function of add-back energy. Area under peak in arbitrary units.



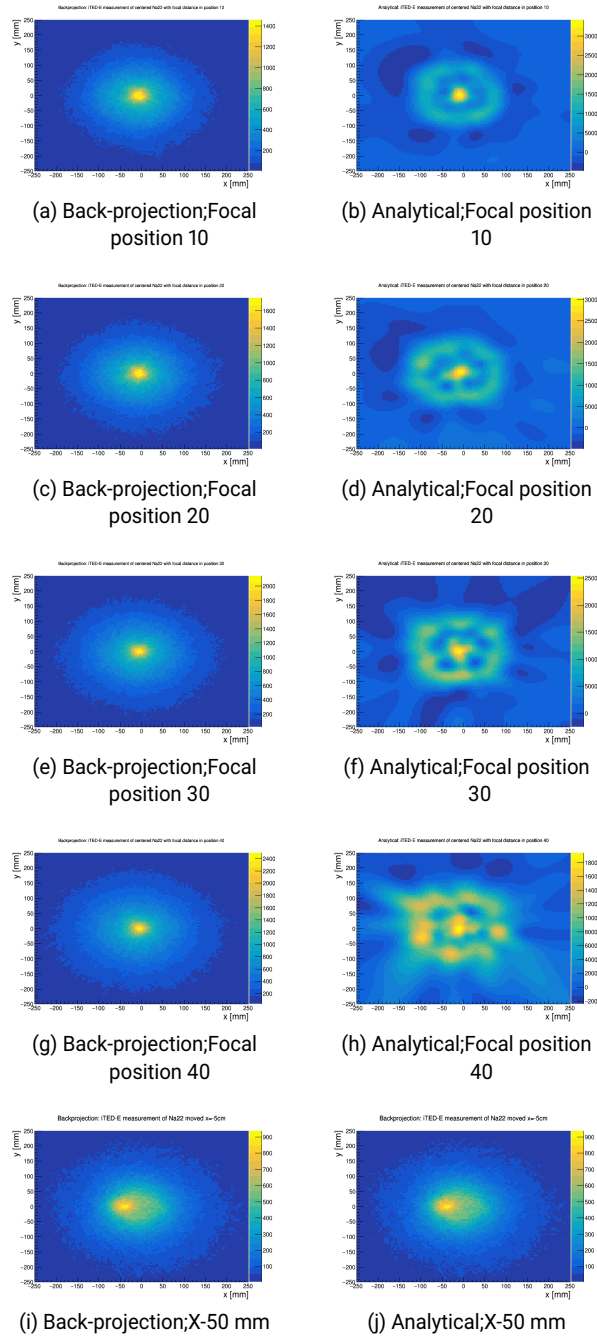


Figure B.2: Complementary imaging results of *i*-TED-E illustrating the effects of different algorithms, different source positions, and difference focal distances.



CSV : GEN-d21c-d2af-ba88-99ce-da2f-70ae-e905-5e92

DIRECCIÓN DE VALIDACIÓN : <https://portafirmas.redsara.es/pf/valida>

FIRMANTE(1) : BERNARDO BERNARDINO GAMEIRO | FECHA : 09/11/2023 15:40 | NOTAS : F

FIRMANTE(2) : JORGE LERENDEGUI MARCO | FECHA : 09/11/2023 18:46 | NOTAS : CF

Código seguro de Verificación : GEN-d21c-d2af-ba88-99ce-da2f-70ae-e905-5e92 | Puede verificar la integridad de este documento en la siguiente dirección :
<https://portafirmas.redsara.es/pf/valida>



CSV : GEN-d21c-d2af-ba88-99ce-da2f-70ae-e905-5e92

DIRECCIÓN DE VALIDACIÓN : <https://portafirmas.redsara.es/pf/valida>

FIRMANTE(1) : BERNARDO BERNARDINO GAMEIRO | FECHA : 09/11/2023 15:40 | NOTAS : F

FIRMANTE(2) : JORGE LERENDEGUI MARCO | FECHA : 09/11/2023 18:46 | NOTAS : CF

SOFTWARE DEVELOPED

Over time, the importance of computers in research has risen, and has undoubtedly become a vital resource in nuclear physics. The field that birthed from their prominence, scientific computing, which had traditionally concerned itself with numerical methods [52, Abstract] and [53], has evolved to encompass High Performance Computing (HPC), network infrastructure, and data management, [53]. As such, the researcher must also evolve in order to reliably and effectively perform their work, [54, Foreword].

This chapter includes changes to the software stack, whether in development or already implemented, and that stemmed from the development of the current thesis project.

C.1 SCIENTIFIC DATA MANAGEMENT

When using a simple γ -ray detector with sources in laboratory, it is important to record important experimental information such as the source, the distance to the source, the threshold and so on and so forth. This, usually, consists in little information that may be easy to associate with the data. However, when using a more complex detection system, such as the multi *i-TED*, the amount of information referent to each measurement increases significantly: instead of a detector, there are 4 modules; instead of a threshold, there is one per pixel; there are coincidence windows at the level of the pixels within a plane, of the planes within a module, and between the modules; there are different algorithms for timestamp calculation, position reconstruction, and Compton imaging. Overall, there is much more information that must be stored with the data.

In order to address this issue, a system is being developed in order to save the information needed as metadata. The Python module *In-take*, [55], was selected for its customization, ease of integration with Python, and for its abstraction of the functions that interact with data by providing a consistent Application Programming Interface (API).

In-take is based on the concept of catalogs. A catalog is a YAML file which includes the path to the data, how to open the data, and the metadata. One such example is included in C.1. Catalogs can also have other catalogs as entries, allowing for hierarchical structures of data.

```
---
{data_name:string}:
  description: {description:string}
  driver: {csv/root/ldat:string}
```



CSV : GEN-d21c-d2af-ba88-99ce-da2f-70ae-e905-5e92

DIRECCIÓN DE VALIDACIÓN : <https://portafirmas.redsara.es/pf/valida>

FIRMANTE(1) : BERNARDO BERNARDINO GAMEIRO | FECHA : 09/11/2023 15:40 | NOTAS : F

FIRMANTE(2) : JORGE LERENDEGUI MARCO | FECHA : 09/11/2023 18:46 | NOTAS : CF

```

args:
  urlpath: {path/to/file:string}
  csv_kwargs:
    header: null
    names: [{"0", "DetectorNumber", "E_s", "X_s", "Y_s", "Z_s",
             "E_a", "X_a", "Y_a", "Z_a", "dt", "ts"}: list of
             strings}
metadata:
  date: {date of measurement:YYYYmddHHMMSS}
  source: {source for measurement:string}
  background: {if any source has been used as background:
               string}
  position:
    x: {x of source:float}
    y: {y of source:float}
    z: {z of source:float}
  detector:
    id: {iTED-E/iTED-A/multi iTED:string}
    offset: {distance between planes:float}
  location: {CMAM/n_ToF/IFIC:string}
  time: {time in seconds:float}
  configuration:
    threshold: {887/888/88C:string}
    version: {version of threshold (important for 88C):
              string}
    cw: {time in nanoseconds:float}
    timing: {timing algorithm:float}
  acquisition:
    pc: {itedws/itedws2/itedws3:string}
  processing:
    pc: {itedws/itedws2/itedws3:string}
    version: {parallelsingles2tree_auto/parallelsingles2
              tree/parallelsingles2tree_lite:string}
---
```

To be able to open different types of data, Intake uses drivers. Drivers are Python classes with common methods for getting the data schema; to import it to different data structures, such as arrays or dataframes; and to import the data lazily with Dask, [56], facilitating the use of distributed computing for Big Data. This makes it so that, regardless of the data type used for storage, the same methods are used for IO. An example of how to access data and metadata is included in C.1.

```

import intake, pandas, dask
catalog = intake.open_catalog('example_tests.yml')
list(catalog)
# ['X_5_1_100', 'X_5_2_100', 'X_5_1_200', 'X_5_1_250']
catalog['X_5_1_100'].metadata
# returns metadata as dictionary
catalog['X_5_1_100'].read()
# returns data as pandas dataframe
catalog['X_5_1_100'].to_dask()
# returns data as dask dataframe
```



CSV : GEN-d21c-d2af-ba88-99ce-da2f-70ae-e905-5e92

DIRECCIÓN DE VALIDACIÓN : <https://portafirmas.redsara.es/pf/valida>

FIRMANTE(1) : BERNARDO BERNARDINO GAMEIRO | FECHA : 09/11/2023 15:40 | NOTAS : F

FIRMANTE(2) : JORGE LERENDEGUI MARCO | FECHA : 09/11/2023 18:46 | NOTAS : CF

Lastly, Intake has a server function which allows connecting to a remote catalog instead of a local one. It includes several features such as combining different catalogs in different remote locations; access to cloud infrastructure such as AWS S3, Azure Datalake or with private ssh/sftp servers; and a sharing functionality which allows publishing datasets.

C.2 CALIBRATION SOFTWARE

Calibration is a fundamental part of any measurement in scientific context, and one of the most basic requirements of any radiation or particle detector in a nuclear physics experiment. In γ -ray spectroscopy, this requirement gains importance when using detectors in coincidence to reconstruct the initial energy, and even more so when the calibrated energy is used to reconstruct an image, as is the case in Compton imaging. In this situation, a deviation in the calibration means more than a deviated energy peak: it means a broadening of the energy peak in coincidence between the scatterer and absorber, it means drifts between the different coincidence energy peaks with different absorbers, and as a consequence a poorer image reconstruction.

For a Compton camera the proper calibration of energies in the Compton plateau is of the utmost importance because those are the energy ranges that will be reconstructed into full-energy absorption peaks in coincidence.

As such, in order to calibrate the detectors over a wide range of energies in conditions as similar as possible, measurements of ^{152}Eu were performed. This isotope has several peaks that can be used for calibration from as low as 122 keV to 1408 keV, [57]. As it had been previously established, [41], the calibration curve used was a second order polynomial.

Furthermore, with 25 individual detectors to calibrate, corresponding to the 20 crystals of the multi *i*-TED and 5 of *i*-TED-E, it isn't practical to do it with common solutions which focus on just one detector. As such, an interface was developed to facilitate this Sisyphian task.

c.2.1 *Developed version*

Leveraging the widget capabilities of Jupyter and the data analysis tools tailored for nuclear and particle physics of PyROOT, the interface of [Figure C.1](#) was developed. This interface has several features which make the calibration easier and quicker:

- Use of multiple measurements
- Background subtraction
- Normalization of spectra



CSV : GEN-d21c-d2af-ba88-99ce-da2f-70ae-e905-5e92

DIRECCIÓN DE VALIDACIÓN : <https://portafirmas.redsara.es/pf/valida>

FIRMANTE(1) : BERNARDO BERNARDINO GAMEIRO | FECHA : 09/11/2023 15:40 | NOTAS : F

FIRMANTE(2) : JORGE LERENDEGUI MARCO | FECHA : 09/11/2023 18:46 | NOTAS : CF

- Uses PyROOT for fitting peaks
- Allows different polynomial fits for the background near a peak
- Takes into account and saves the peak standard deviation for the resolution
- The data is saved with the identification of the respective crystal
- Queries the IAEA isotope database for the most prominent γ -rays emitted
- Allows for quickly changing a fit to another crystal and refit

As the crystals and electronic chains are similar for all *i*-TED modules, in many cases, the interval, the background and the characteristics of the peak are similar. As such, it is possible to obtain the fit in one crystal by using the parameters resulting from the fit in another, without the need to redefine the interval or the initial parameters. Leveraging this functionality, the calibration becomes less time-consuming.

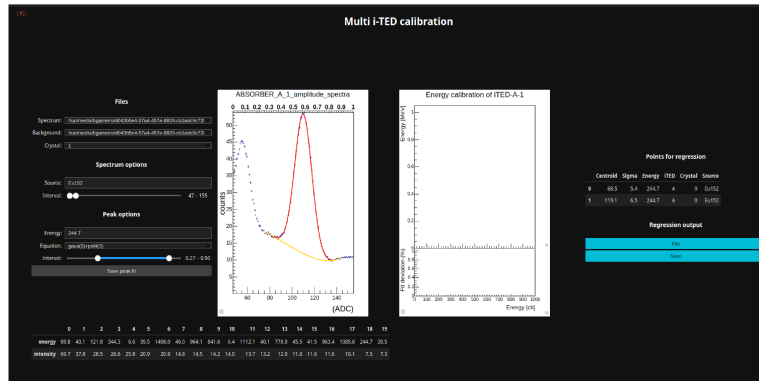


Figure C.1: Calibration interface developed for *i*-TED.

c.2.2 InterSpec

One previously existing tool, illustrated in [Figure C.2](#), that was also extensively used for calibration during the development of this project is InterSpec developed by [SNL](#). This tool includes several features such as search for possible γ -ray energies given the source used:

- Use of multiple measurements
- Background subtraction
- Normalization of spectra
- Search for decay energies and even some nuclear reactions



CSV : GEN-d21c-d2af-ba88-99ce-da2f-70ae-e905-5e92

DIRECCIÓN DE VALIDACIÓN : <https://portafirmas.redsara.es/pf/valida>

FIRMANTE(1) : BERNARDO BERNARDINO GAMEIRO | FECHA : 09/11/2023 15:40 | NOTAS : F

FIRMANTE(2) : JORGE LERENDEGUI MARCO | FECHA : 09/11/2023 18:46 | NOTAS : CF

- Allows different polynomial fits for the background near a peak
- Allows for fitting multiple peaks at the same time

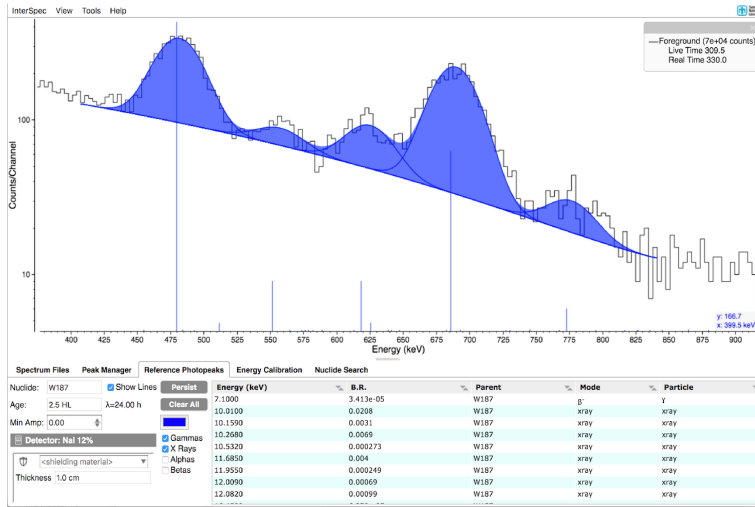


Figure C.2: InterSpec calibration interface developed by SNL. Image from [58].

However, the most important feature that contributed to the increase efficiency of calibration is the ease of fitting peaks just by double-clicking them. The software automatically chooses an interval and initial parameters for the fit of both the peak and background. If the source (or sources) being measured were provided, it also suggests the energy for the peak. Any of the parameters described can also be altered and fine-tuned if needed, although the default parameters worked correctly through-out the use of the program.

C.3 REWRITE OF SINGLES2TREE

The `singles2tree` program was developed in order to generate ROOT files from the binary data files in which the data is originally written. Several versions of this code were created with different algorithms for timing and position reconstruction. As part of this thesis, and with the objective of streamlining the process, using the concept of data pipeline in mind, this code was rewritten in Python using tools commonly used for data analysis and signal processing.

c.3.1 *i-TED's data processing*

The *i-TED* acquisition is built on top of the PETSys' software. This software is responsible for controlling the acquisition modules, the ASICs, and the SiPM.

CSV : GEN-d21c-d2af-ba88-99ce-da2f-70ae-e905-5e92

DIRECCIÓN DE VALIDACIÓN : <https://portafirmas.redsara.es/pf/valida>

FIRMANTE(1) : BERNARDO BERNARDINO GAMEIRO | FECHA : 09/11/2023 15:40 | NOTAS : F

FIRMANTE(2) : JORGE LERENDEGUI MARCO | FECHA : 09/11/2023 18:46 | NOTAS : CF

At the **SiPM** level, it sets the bias voltage and the thresholds. According to PETSys' manuals, there are three thresholds that can be set on a per-pixel basis, corresponding to each number of a given threshold configuration, for example the 888 configuration has the value 8, in arbitrary units, for each of the thresholds. The first two thresholds had already been optimized to a state where the last threshold, t_E , has the most significant impact. The effect of this threshold was studied in the current thesis' project, [Section 4.2.2](#).

At the **ASIC** level, the time synchronization between different pixels is set, and the charge collected, in arbitrary units, by each pixel is calculated. From here, the timestamp, charge and pixel ID of each pulse is transmitted to the acquisition modules. The acquisition modules ensure the time synchronization between different **ASICs**, which correspond to different **SiPMs**, returning the data, consisting of the timestamp, the charge and pixel ID, which is written to a binary `.ldat` file in list mode.

The information in the `.ldat` isn't used directly, needing first to be pre-processed and stored in a ROOT file, which is easier to work with. This is represented in [Figure C.3](#).

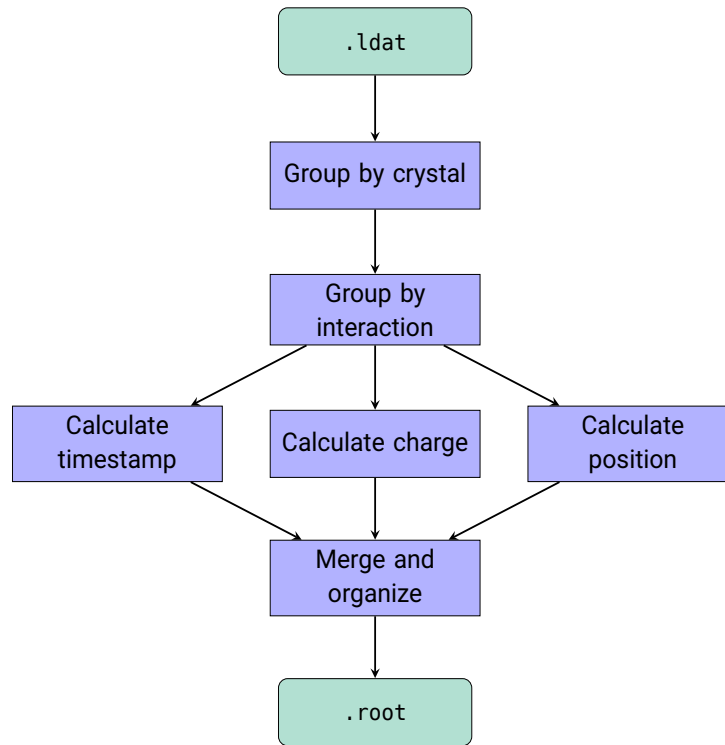


Figure C.3: Data pipeline for **i-TED**.

In the `singles2tree` code, that transforms the binary to ROOT files, grouping by interaction is done by using a non-overlapping window of fixed



time between 100 and 250 ns, as explored in [Section 4.3](#). Being non-overlapping, it means that once the sum charge of the entries inside the window are over the threshold, an interaction is computed and the window is moved to the first entry after the interaction. The computation of position and timestamp were addressed in [Section 4.2.1.1](#) and [Section 4.2.3.2](#), respectively. Finally, in the `singles2tree` code, a second coincidence window is used in order to group single events into coincidence events so that they can be used for Compton imaging.

c.3.2 Software upgrades

The previous working version of `singles2tree` has been written in C++. A new version is being written in Python with the characteristics described below. Currently, there is a working version written with Dask that takes significantly longer than its established counterpart.

DATA PIPELINE: PREFECT Currently, different versions for calculating the position and the timestamp exist. By organizing this preprocessing as a Prefect data pipeline, switching between different versions at the level of the component becomes trivial, allowing greater control than versioning at the level of the whole program. It also allows the use of analytics such as keeping track of the time of each step of where it may fail, as well as deal with exceptions.

BIG DATA AND DISTRIBUTION: DASK As seen in [Table 4.3](#), a background measurement has about 415 MB/min with the threshold configuration 88c, which implies a two hours background measurement will have almost 50 GB and much more if a source is present. Those values are bigger than the memory found in most systems, entering the domain of Big Data. The module Dask allows for dealing with out-of-memory datasets, by doing lazy computation, meaning that the data is only loaded if it is used for computation; by computing the execution task graph, which optimizes the sequence of execution; and by distributing parallel task, either locally or remotely in a cluster.

PERFORMANCE: NUMBA, RAPIDS AND CUPY Lastly, as it would be interesting to have *i-TED*, a γ -ray imager, working in real time, studies into the performance are being done in order to validate the possibility of real-time imaging. Such studies are carried based on performance metrics which identify the current bottlenecks. Common solutions include the compilation of specific functions either for CPU or GPU.

c.3.3 Proposed software upgrades

PILE UP Algorithms have been proposed in order to counter the pile up effect. In most detectors, this needs to be done one the basis of the



CSV : GEN-d21c-d2af-ba88-99ce-da2f-70ae-e905-5e92

DIRECCIÓN DE VALIDACIÓN : <https://portafirmas.redsara.es/pf/valida>

FIRMANTE(1) : BERNARDO BERNARDINO GAMEIRO | FECHA : 09/11/2023 15:40 | NOTAS : F

FIRMANTE(2) : JORGE LERENDEGUI MARCO | FECHA : 09/11/2023 18:46 | NOTAS : CF

temporal distribution of charge. However, with detectors which also record the position of the interaction, this can be done on the time and spacial distribution of charge.

CHARGE FITS Currently, the charge of an interaction is equal to the sum of the charges of its entries. However, algorithms could be developed in order to compute the charge based on the temporal and spacial distribution of charge, akin to how the area of the Gaussian fit is taken in spectroscopy instead of the numerical sum of the events.

DEFINITION OF INTERACTION As stated previously, an interaction is defined as a group of entries within a given time window, without overlapping in time with a previous interaction, whose sum charge is over the threshold. A different approach could entail maximizing the sum charge instead of taking the first series of entries that is over the threshold.



CSV : GEN-d21c-d2af-ba88-99ce-da2f-70ae-e905-5e92

DIRECCIÓN DE VALIDACIÓN : <https://portafirmas.redsara.es/pf/valida>

FIRMANTE(1) : BERNARDO BERNARDINO GAMEIRO | FECHA : 09/11/2023 15:40 | NOTAS : F

FIRMANTE(2) : JORGE LERENDEGUI MARCO | FECHA : 09/11/2023 18:46 | NOTAS : CF

BIBLIOGRAPHY

- [1] *Group of Gamma-ray and Neutron Spectroscopy*. <http://webgamma.ific.uv.es/gamma/>.
- [2] G. Tagliente et al. "The $^{93}\text{Zr}(n, \gamma)$ reaction up to 8 keV neutron energy." In: *Phys. Rev. C* 87 (1 2013), p. 014622. DOI: [10.1103/PhysRevC.87.014622](https://doi.org/10.1103/PhysRevC.87.014622). URL: <https://link.aps.org/doi/10.1103/PhysRevC.87.014622>.
- [3] C. Domingo-Pardo et al. "New measurement of neutron capture resonances in Bi209." In: *Physical Review C* 74.2, 025807 (2006), p. 025807. DOI: [10.1103/PhysRevC.74.025807](https://doi.org/10.1103/PhysRevC.74.025807). arXiv: [nucl-ex/0610040](https://arxiv.org/abs/nucl-ex/0610040) [nucl-ex].
- [4] Christian Iliadis. *Nuclear physics of stars*. en. 2nd ed. Weinheim, Germany: Wiley-VCH Verlag, 2015.
- [5] F. Käppeler. "Stellar neutron capture rates and the s process." In: *EPJ Web of Conferences* 21 (2012), p. 03006. ISSN: 2100-014X. DOI: [10.1051/epjconf/20122103006](https://doi.org/10.1051/epjconf/20122103006).
- [6] *Experimental Astrophysics: Neutron-induced reactions*. <https://exp-astro.de/index.php?lang=en&id=researchNeutron>.
- [7] C. Guerrero et al. "Performance of the neutron time-of-flight facility n_TOF at CERN." In: *The European Physical Journal A* 49.2 (2013). DOI: [10.1140/epja/i2013-13027-6](https://doi.org/10.1140/epja/i2013-13027-6). URL: <https://doi.org/10.1140/epja/i2013-13027-6>.
- [8] B. Fernández, M. Macías, C. Guerrero, M. A. Millán-Callado, T. Rodríguez-Gonzalez, J. M. Quesada, J. Gómez-Camacho, and J. Praena. "HiSPANoS facility and the new neutron beam line for TOF measurements at the Spanish National Accelerator Lab (CNA)." In: *J. Phys. Conf. Ser.* 1643.1 (2020), p. 012033. ISSN: 1742-6596. DOI: [10.1088/1742-6596/1643/1/012033](https://doi.org/10.1088/1742-6596/1643/1/012033).
- [9] C. Weiß et al. "The new vertical neutron beam line at the CERN n_TOF facility design and outlook on the performance." In: *Nuclear Instruments and Methods in Physics Research Section A: Accelerators, Spectrometers, Detectors and Associated Equipment* 799 (2015), pp. 90–98. DOI: [10.1016/j.nima.2015.07.027](https://doi.org/10.1016/j.nima.2015.07.027). URL: <https://doi.org/10.1016/j.nima.2015.07.027>.
- [10] Y.H. Chen et al. "Characterization of the n_TOF EAR-2 neutron beam." In: *EPJ Web of Conferences* 146 (2017). Ed. by A. Plompen, F.-J. Hamsch, P. Schillebeeckx, W. Mondelaers, J. Heyse, S. Kopecky, P. Siegler, and S. Oberstedt, p. 03020. DOI: [10.1051/epjconf/201714603020](https://doi.org/10.1051/epjconf/201714603020). URL: <https://doi.org/10.1051/epjconf/201714603020>.

CSV : GEN-d21c-d2af-ba88-99ce-da2f-70ae-e905-5e92

DIRECCIÓN DE VALIDACIÓN : <https://portafirmas.redsara.es/pf/valida>

FIRMANTE(1) : BERNARDO BERNARDINO GAMEIRO | FECHA : 09/11/2023 15:40 | NOTAS : F

FIRMANTE(2) : JORGE LERENDEGUI MARCO | FECHA : 09/11/2023 18:46 | NOTAS : CF



- [11] V. Alcayne et al. "A segmented total energy detector (sTED) for (n, γ) cross section measurements at n_TOF EAR2." In: *EPJ Web of Conferences* 284 (2023). Ed. by C.M. Mattoon, R. Vogt, J. Escher, and I. Thompson, p. 01043. doi: [10.1051/epjconf/202328401043](https://doi.org/10.1051/epjconf/202328401043). URL: <https://doi.org/10.1051/epjconf/202328401043>.
- [12] Christian Fabjan and Herwig Schopper. *Particle Physics Reference Library*. Vol. 2. Springer International Publishing, 2020. doi: [10.1007/978-3-030-35318-6](https://doi.org/10.1007/978-3-030-35318-6).
- [13] J. Anthony Seibert and John M. Boone. "X-Ray Imaging Physics for Nuclear Medicine Technologists. Part 2: X-Ray Interactions and Image Formation." In: *J. Nucl. Med. Technol.* 33.1 (2005), pp. 3–18. ISSN: 0091-4916. URL: <https://tech.snmjournals.org/content/33/1/3>.
- [14] Glenn F. Knoll. *Interaction of fast electrons*. Wiley, 2010. ISBN: 978-0-470-13148-0. URL: <https://www.wiley.com/en-fr/Radiation+Detection+and+Measurement%2C+4th+Edition-p-9780470131480>.
- [15] C. Guerrero et al. "The n_TOF Total Absorption Calorimeter for neutron capture measurements at CERN." In: *Nuclear Instruments and Methods in Physics Research Section A: Accelerators, Spectrometers, Detectors and Associated Equipment* 608.3 (2009), pp. 424–433. doi: [10.1016/j.nima.2009.07.025](https://doi.org/10.1016/j.nima.2009.07.025). URL: <https://doi.org/10.1016/j.nima.2009.07.025>.
- [16] U Abbondanno et al. "New experimental validation of the pulse height weighting technique for capture cross-section measurements." In: *Nuclear Instruments and Methods in Physics Research Section A: Accelerators, Spectrometers, Detectors and Associated Equipment* 521.2-3 (2004), pp. 454–467. doi: [10.1016/j.nima.2003.09.066](https://doi.org/10.1016/j.nima.2003.09.066). URL: <https://doi.org/10.1016/j.nima.2003.09.066>.
- [17] Reinhard Stock. *Encyclopedia of Nuclear Physics and its Applications*. Weinheim, Germany: Wiley, 2013. ISBN: 978-3-527-40742-2. URL: <https://www.wiley.com/en-be/Encyclopedia+of+Nuclear+Physics+and+its+Applications-p-9783527407422>.
- [18] William W. Moses. "Current trends in scintillator detectors and materials." In: *Nucl. Instrum. Methods Phys. Res., Sect. A* 487.1 (2002), pp. 123–128. ISSN: 0168-9002. doi: [10.1016/S0168-9002\(02\)00955-5](https://doi.org/10.1016/S0168-9002(02)00955-5).
- [19] R.J. Cooper, M. Amman, and K. Vetter. "High resolution gamma-ray spectroscopy at high count rates with a prototype High Purity Germanium detector." In: *Nuclear Instruments and Methods in Physics Research Section A: Accelerators, Spectrometers, Detectors and Associated Equipment* 886 (2018), pp. 1–6. doi: [10.1016/j.nima.2017.12.053](https://doi.org/10.1016/j.nima.2017.12.053). URL: <https://doi.org/10.1016/j.nima.2017.12.053>.



CSV : GEN-d21c-d2af-ba88-99ce-da2f-70ae-e905-5e92

DIRECCIÓN DE VALIDACIÓN : <https://portafirmas.redsara.es/pf/valida>

FIRMANTE(1) : BERNARDO BERNARDINO GAMEIRO | FECHA : 09/11/2023 15:40 | NOTAS : F

FIRMANTE(2) : JORGE LERENDEGUI MARCO | FECHA : 09/11/2023 18:46 | NOTAS : CF

- [20] A. Borella, G. Aerts, F. Gunsing, M. Moxon, P. Schillebeeckx, and R. Wynants. "The use of C6D6 detectors for neutron induced capture cross-section measurements in the resonance region." In: *Nucl. Instrum. Methods Phys. Res., Sect. A* 577.3 (2007), pp. 626–640. ISSN: 0168-9002. DOI: [10.1016/j.nima.2007.03.034](https://doi.org/10.1016/j.nima.2007.03.034).
- [21] R. Plag, M. Heil, F. Käppeler, P. Pavlopoulos, R. Reifarth, and K. Wisshak. "An optimized C6D6 detector for studies of resonance-dominated (n, γ) cross-sections." In: *Nuclear Instruments and Methods in Physics Research Section A: Accelerators, Spectrometers, Detectors and Associated Equipment* 496.2-3 (2003), pp. 425–436. DOI: [10.1016/s0168-9002\(02\)01749-7](https://doi.org/10.1016/s0168-9002(02)01749-7). URL: [https://doi.org/10.1016/s0168-9002\(02\)01749-7](https://doi.org/10.1016/s0168-9002(02)01749-7).
- [22] A. Giaz et al. "The CLYC-6 and CLYC-7 response to γ -rays, fast and thermal neutrons." In: *Nuclear Instruments and Methods in Physics Research Section A: Accelerators, Spectrometers, Detectors and Associated Equipment* 810 (2016), pp. 132–139. ISSN: 0168-9002. DOI: <https://doi.org/10.1016/j.nima.2015.11.119>. URL: <https://www.sciencedirect.com/science/article/pii/S0168900215015065>.
- [23] V.Lj. Ljubenov and P. M. Marinkovic. "Applicability of Compton imaging in nuclear decommissioning activities." In: International Yugoslav Nuclear Society Conference (YUNSC-2002). ENGINEERING. Yugoslavia: Institute of Nuclear Sciences VINCA, Belgrade, Yugoslavia, 2002. ISBN: 86-7306-062-1. URL: http://inis.iaea.org/search/search.aspx?orig_q=RN:38048868.
- [24] Raj Kumar Parajuli, Makoto Sakai, Ramila Parajuli, and Mutsumi Tashiro. "Development and Applications of Compton Camera—A Review." In: *Sensors* 22.19 (2022), p. 7374. ISSN: 1424-8220. DOI: [10.3390/s22197374](https://doi.org/10.3390/s22197374).
- [25] *Animation of i-TED's working principle*. <https://hymnserc.ific.uv.es/ited/>.
- [26] S. Vandenberghe, E. Mikhaylova, E. D'Hoe, P. Mollet, and J. S. Karp. "Recent developments in time-of-flight PET." In: *EJNMMI Physics* 3.1 (2016). DOI: [10.1186/s40658-016-0138-3](https://doi.org/10.1186/s40658-016-0138-3). URL: <https://doi.org/10.1186/s40658-016-0138-3>.
- [27] P. Olleros, L. Caballero, C. Domingo-Pardo, V. Babiano, I. Ladarescu, D. Calvo, P. Gramage, E. Nacher, J.L. Tain, and A. Tolosa. "On the performance of large monolithic LaCl₃(Ce) crystals coupled to pixelated silicon photosensors." In: *Journal of Instrumentation* 13.03 (2018), P03014–P03014. DOI: [10.1088/1748-0221/13/03/p03014](https://doi.org/10.1088/1748-0221/13/03/p03014). URL: <https://doi.org/10.1088/1748-0221/13/03/p03014>.



CSV : GEN-d21c-d2af-ba88-99ce-da2f-70ae-e905-5e92

DIRECCIÓN DE VALIDACIÓN : <https://portafirmas.redsara.es/pf/valida>

FIRMANTE(1) : BERNARDO BERNARDINO GAMEIRO | FECHA : 09/11/2023 15:40 | NOTAS : F

FIRMANTE(2) : JORGE LERENDEGUI MARCO | FECHA : 09/11/2023 18:46 | NOTAS : CF

- [28] V. Babiano, L. Caballero, D. Calvo, I. Ladarescu, P. Olleros, and C. Domingo-Pardo. "γ-Ray position reconstruction in large monolithic LaCl₃(Ce) crystals with SiPM readout." In: *Nuclear Instruments and Methods in Physics Research Section A: Accelerators, Spectrometers, Detectors and Associated Equipment* 931 (2019), pp. 1–22. ISSN: 0168-9002. DOI: <https://doi.org/10.1016/j.nima.2019.03.079>. URL: <https://www.sciencedirect.com/science/article/pii/S0168900219304218>.
- [29] V. Babiano, J. Balibrea, L. Caballero, D. Calvo, I. Ladarescu, J. Lerenegui, S. Mira Prats, and C. Domingo-Pardo. "First i-TED demonstrator: A Compton imager with Dynamic Electronic Collimation." In: *Nuclear Instruments and Methods in Physics Research Section A: Accelerators, Spectrometers, Detectors and Associated Equipment* 953 (2020), p. 163228. ISSN: 0168-9002. DOI: <https://doi.org/10.1016/j.nima.2019.163228>. URL: <https://www.sciencedirect.com/science/article/pii/S0168900219315104>.
- [30] J. Balibrea-Correa, J. Lerenegui-Marco, V. Babiano-Suárez, L. Caballero, D. Calvo, I. Ladarescu, P. Olleros-Rodríguez, and C. Domingo-Pardo. "Machine Learning aided 3D-position reconstruction in large LaCl₃ crystals." In: *Nuclear Instruments and Methods in Physics Research Section A: Accelerators, Spectrometers, Detectors and Associated Equipment* 1001 (2021), p. 165249. ISSN: 0168-9002. DOI: <https://doi.org/10.1016/j.nima.2021.165249>. URL: <https://www.sciencedirect.com/science/article/pii/S0168900221002333>.
- [31] V. Babiano-Suárez et al. "Imaging neutron capture cross sections: i-TED proof-of-concept and future prospects based on Machine-Learning techniques." In: *The European Physical Journal A* 57.6 (2021). DOI: [10.1140/epja/s10050-021-00507-7](https://doi.org/10.1140/epja/s10050-021-00507-7). URL: <https://doi.org/10.1140/epja/s10050-021-00507-7>.
- [32] C. Domingo-Pardo. "i-TED: A novel concept for high-sensitivity (n, γ) cross-section measurements." In: *Nuclear Instruments and Methods in Physics Research Section A: Accelerators, Spectrometers, Detectors and Associated Equipment* 825 (2016), pp. 78–86. ISSN: 0168-9002. DOI: <https://doi.org/10.1016/j.nima.2016.04.002>. URL: <https://www.sciencedirect.com/science/article/pii/S0168900216301619>.
- [33] Ion Ladarescu, Victor Babiano, Javier Balibrea, Luis Caballero, David Calvo, Cesar Domingo-Pardo, Jorge Lerenegui, and Pablo Olleros. "Gamma-ray position reconstruction in large lanthanum-halide crystals with SiPM readout: analytical vs. neural-network algorithms." In: *2019 IEEE Nuclear Science Symposium and Medical Imaging Conference (NSS/MIC)*. IEEE, pp. 2019–02. doi: [10.1109/NSS/MIC42101.2019.9059754](https://doi.org/10.1109/NSS/MIC42101.2019.9059754).



CSV : GEN-d21c-d2af-ba88-99ce-da2f-70ae-e905-5e92

DIRECCIÓN DE VALIDACIÓN : <https://portafirmas.redsara.es/pf/valida>

FIRMANTE(1) : BERNARDO BERNARDINO GAMEIRO | FECHA : 09/11/2023 15:40 | NOTAS : F

FIRMANTE(2) : JORGE LERENEGUI MARCO | FECHA : 09/11/2023 18:46 | NOTAS : CF

- [34] Efthymios Lamprou, Antonio J. Gonzalez, Filomeno Sanchez, and Jose M. Benlloch. "Exploring TOF capabilities of PET detector blocks based on large monolithic crystals and analog SiPMs." In: *Physica Medica* 70 (2020), pp. 10–18. ISSN: 1120-1797. DOI: <https://doi.org/10.1016/j.ejmp.2019.12.004>. URL: <https://www.sciencedirect.com/science/article/pii/S1120179719305253>.
- [35] *LaCl3 from Halida-Crylink*. <https://www.halide-crylink.com/chloride-crystal/lac13-crystal/>.
- [36] J. Leredegui-Marco et al. "New detection systems for an enhanced sensitivity in key stellar (n, γ) measurements." In: *EPJ Web Conf.* 279 (2023), p. 13001. ISSN: 2100-014X. DOI: [10.1051/epjconf/202327913001](https://doi.org/10.1051/epjconf/202327913001).
- [37] G I Klenov and V S Khoroshkov. "Hadron therapy: history, status, prospects." In: *Physics-Uspekhi* 59.8 (2016), pp. 807–825. DOI: [10.3367/ufne.2016.06.037823](https://doi.org/10.3367/ufne.2016.06.037823). URL: <https://doi.org/10.3367/ufne.2016.06.037823>.
- [38] J. Balibrea-Correa, J. Leredegui-Marco, I. Ladarescu, C. Guerrero, T. Rodríguez-González, M. C. Jiménez-Ramos, B. Fernández-Martínez, and C. Domingo-Pardo. "Hybrid in-beam PET- and Compton prompt-gamma imaging aimed at enhanced proton-range verification." In: *The European Physical Journal Plus* 137.11 (2022). DOI: [10.1140/epjp/s13360-022-03414-y](https://doi.org/10.1140/epjp/s13360-022-03414-y). URL: <https://doi.org/10.1140/epjp/s13360-022-03414-y>.
- [39] L. Caballero, F. Albiol Colomer, A. Corbi Bellot, C. Domingo-Pardo, J.L. Leganés Nieto, J. Agramunt Ros, P. Contreras, M. Monserate, P. Olleros Rodríguez, and D.L. Pérez Magán. "Gamma-ray imaging system for real-time measurements in nuclear waste characterisation." In: *Journal of Instrumentation* 13.03 (2018), P03016–P03016. DOI: [10.1088/1748-0221/13/03/p03016](https://doi.org/10.1088/1748-0221/13/03/p03016). URL: <https://doi.org/10.1088/1748-0221/13/03/p03016>.
- [40] C.A. *El Cabril*. [Online; accessed 4. Sep. 2023]. 2023. URL: <https://www.enresa.es/esp/inicio/actividades-y-proyectos/ca-el-cabril>.
- [41] Víctor Babiano Suárez. "High resolution $^{80}\text{Se}(n, \gamma)$ cross section measurement at CERN n_TOF and development of the novel i-TED detection system." PhD thesis. 2022.
- [42] J. Leredegui-Marco et al. "New detection systems for an enhanced sensitivity in key stellar (n, γ) measurements." In: *EPJ Web of Conferences* 279 (2023). Ed. by S. Freeman, C. Lederer-Woods, A. Manna, and A. Mengoni, p. 13001. DOI: [10.1051/epjconf/202327913001](https://doi.org/10.1051/epjconf/202327913001). URL: <https://doi.org/10.1051/epjconf/202327913001>.



CSV : GEN-d21c-d2af-ba88-99ce-da2f-70ae-e905-5e92

DIRECCIÓN DE VALIDACIÓN : <https://portafirmas.redsara.es/pf/valida>

FIRMANTE(1) : BERNARDO BERNARDINO GAMEIRO | FECHA : 09/11/2023 15:40 | NOTAS : F

FIRMANTE(2) : JORGE LERENDEGUI MARCO | FECHA : 09/11/2023 18:46 | NOTAS : CF

- [43] G. Daniel, O. Limousin, D. Maier, A. Meuris, and F. Carrel. "Compton imaging reconstruction methods: a comparative performance study of direct back-projection, SOE, a new Bayesian algorithm and a new Compton inversion method applied to real data with Caliste." In: *EPJ Web of Conferences* 225 (2020). Ed. by A. Lyoussi, M. Giot, M. Carette, I. Jenčič, C. Reynard-Carette, L. Vermeeren, L. Snoj, and P. Le Dû, p. 06006. doi: [10.1051/epjconf/202022506006](https://doi.org/10.1051/epjconf/202022506006). URL: <https://doi.org/10.1051/epjconf/202022506006>.
- [44] Jorge Lerendegui-Marco, Javier Balibrea-Correa, Víctor Babiano-Suárez, Ion Ladarescu, and César Domingo-Pardo. "Towards machine learning aided real-time range imaging in proton therapy." In: *Scientific Reports* 12.1 (2022). doi: [10.1038/s41598-022-06126-6](https://doi.org/10.1038/s41598-022-06126-6). URL: <https://doi.org/10.1038/s41598-022-06126-6>.
- [45] T Tomitani and M Hirasawa. "Image reconstruction from limited angle Compton camera data." In: *Physics in Medicine and Biology* 47.12 (2002), pp. 2129–2145. doi: [10.1088/0031-9155/47/12/309](https://doi.org/10.1088/0031-9155/47/12/309). URL: <https://doi.org/10.1088/0031-9155/47/12/309>.
- [46] M. S. Bandstra et al. "DETECTION AND IMAGING OF THE CRAB NEBULA WITH THE NUCLEAR COMPTON TELESCOPE." In: *The Astrophysical Journal* 738.1 (2011), p. 8. doi: [10.1088/0004-637x/738/1/8](https://doi.org/10.1088/0004-637x/738/1/8). URL: <https://doi.org/10.1088/0004-637x/738/1/8>.
- [47] Rene Brun et al. *root-project/root: v6.18/02*. 2019. doi: [10.5281/ZENODO.3895860](https://zenodo.org/record/3895860). URL: <https://zenodo.org/record/3895860>.
- [48] J. Lerendegui-Marco, V. Babiano-Suárez, J. Balibrea-Correa, L. Caballero, D. Calvo, C. Domingo-Pardo, and I. Ladarescu. "i-TED: Compton Imaging and Machine-Learning Techniques for Enhanced Sensitivity Neutron Capture Time-of-flight Measurements." In: *2021 IEEE Nuclear Science Symposium and Medical Imaging Conference (NSS/MIC)*. IEEE, 2021, pp. 1–7. doi: [10.1109/NSS/MIC44867.2021.9875461](https://doi.org/10.1109/NSS/MIC44867.2021.9875461).
- [49] Giuseppe Carleo, Ignacio Cirac, Kyle Cranmer, Laurent Daudet, Maria Schuld, Naftali Tishby, Leslie Vogt-Maranto, and Lenka Zdeborová. "Machine learning and the physical sciences." In: *Rev. Mod. Phys.* 91.4 (2019), p. 045002. ISSN: 1539-0756. doi: [10.1103/RevModPhys.91.045002](https://doi.org/10.1103/RevModPhys.91.045002).
- [50] Ian Goodfellow, Yoshua Bengio, and Aaron Courville. *Deep Learning*. <http://www.deeplearningbook.org>. MIT Press, 2016.
- [51] George Em Karniadakis, Ioannis G. Kevrekidis, Lu Lu, Paris Perdikaris, Sifan Wang, and Liu Yang. "Physics-informed machine learning." In: *Nat. Rev. Phys.* 3 (2021), pp. 422–440. ISSN: 2522-5820. doi: [10.1038/s42254-021-00314-5](https://doi.org/10.1038/s42254-021-00314-5).



CSV : GEN-d21c-d2af-ba88-99ce-da2f-70ae-e905-5e92

DIRECCIÓN DE VALIDACIÓN : <https://portafirmas.redsara.es/pf/valida>

FIRMANTE(1) : BERNARDO BERNARDINO GAMEIRO | FECHA : 09/11/2023 15:40 | NOTAS : F

FIRMANTE(2) : JORGE LERENDEGUI MARCO | FECHA : 09/11/2023 18:46 | NOTAS : CF

- [52] René Heinzl. "Concepts for scientific computing." en. PhD thesis. 2007. doi: [10.34726/HSS.2007.9483](https://doi.org/10.34726/HSS.2007.9483). URL: <https://repositum.tuwien.at/handle/20.500.12708/20400>.
- [53] ALBERTO PACE. "TECHNOLOGIES FOR LARGE DATA MANAGEMENT IN SCIENTIFIC COMPUTING." In: *International Journal of Modern Physics C* 25.02 (2014), p. 1430001. doi: [10.1142/s0129183114300012](https://doi.org/10.1142/s0129183114300012). URL: <https://doi.org/10.1142/s0129183114300012>.
- [54] Anthony Scopatz and Kathryn Huff. *Effective Computation in Physics*. en. Sebastopol, CA: O'Reilly Media, 2015.
- [55] *Intake: A general interface for loading data*. <https://github.com/intake/intake>. 2023.
- [56] Dask Development Team. *Dask: Library for dynamic task scheduling*. 2016. URL: <https://dask.org>.
- [57] *NuDat 3*. [Online; accessed 5. Sep. 2023]. July 2023. URL: <https://www.nndc.bnl.gov/nudat3>.
- [58] *InterSpec*. [Online; accessed 3. Sep. 2023]. 2023. URL: <https://sandialabs.github.io/InterSpec>.



CSV : GEN-d21c-d2af-ba88-99ce-da2f-70ae-e905-5e92

DIRECCIÓN DE VALIDACIÓN : <https://portafirmas.redsara.es/pf/valida>

FIRMANTE(1) : BERNARDO BERNARDINO GAMEIRO | FECHA : 09/11/2023 15:40 | NOTAS : F

FIRMANTE(2) : JORGE LERENDEGUI MARCO | FECHA : 09/11/2023 18:46 | NOTAS : CF